Title
Nanopillar Optical Antenna Avalanche Detectors

Author
Senanayake, Pradeep Nuwan

Publication Date
2014

Peer reviewed|Thesis/dissertation

UNIVERSITY OF CALIFORNIA

Los Angeles

Nanopillar Optical Antenna Avalanche Detectors

A dissertation submitted in partial satisfaction of the

requirements for the degree Doctor of Philosophy

in Electrical Engineering

by

Pradeep Nuwan Senanayake

2014

ABSTRACT OF THE DISSERTATION

Nanopillar Optical Antenna Avalanche Detectors

by

Pradeep Nuwan Senanayake

Doctor of Philosophy in Electrical Engineering

University of California, Los Angeles, 2014

Professor Diana L. Huffaker, Chair

Avalanche photodetectors (APDs) are essential components in active imaging systems requiring both ultrafast response times to measure photon time of flight and high gains to detect low photon fluxes. APDs improve system Signal to Noise Ratio by combining photon detection and amplification eliminating the need for front end amplifiers. An emerging trend in active imaging focal plane array technologies is reducing the pixel pitch (detector volume) for higher resolution images. However, there is an inherent trade-off between reduced detector volume and APD figures of merit.

This dissertation will focus on the design, fabrication and electro-optic characterization of a novel detector architecture "3D Nanopillar Optical Antenna Avalanche Detectors" (3D-NOAADs) for shrinking both the absorption and multiplication volumes using III-V nanopillars, while enhancing the optical absorption via a self aligned 3D plasmonic antenna. Wavelength tuning and hybridization of the optical absorption via Surface Plasmon Polariton Bloch Waves (SPP-BWs) and Localized Surface Plasmon Resonances (LSPRs) will be discussed. Photo-generated carrier transport from the

absorption region into the multiplication region and subsequent impact ionization will also be discussed. Single pixel 3D-NOAADs exhibit substantially lower excess noise factors compared to bulk, low breakdown voltages ~ 8 V and gain-bandwidth products > 100 GHz.

The dissertation of Pradeep Nuwan Senanayake is approved.

Robert Candler

Benjamin S. Williams

Shimon Weiss

Diana L. Huffaker, Committee Chair

University of California, Los Angeles

2014

Contents

List of Figures

Acknowledgements

I would like to thank my committee chair Prof. Diana Huffaker for giving me the opportunity to explore this novel area of research on Nanopillar Optical Antenna Avalanche Detectors. Prof. Huffaker has been instrumental in mentoring and focusing my research . I would also like to thank my committee of Prof. Ben Williams, Prof. Shimon Weiss and Prof. Robert Candler for their time and suggestions. Prof. Williams has given me great insights into the physics of plasmonic devices and his students Amir, Ben Burnett and Parthia have been a pleasure to work with.

It takes a village to raise a PhD and I have been fortunate to collaborate with a talented group of researchers in the Huffaker group. I would like to thank Ping-Show and Josh for developing nanopillar growth, Adam for developing nanopillar passivation shells, Andrew for TEM analysis, Chester for device simulations, Alan for his patience in setting up noise measurements, Charles for setting up equipment in the optics lab, Ramesh for building solar cell characterization setups, Clayton for device measurements, Mariko for administrative support and Baolai for his scientific feedback and life wisdom. I would also like to acknowledge the contributions of motivated undergraduate students Nick, Tim, Viet, Gabrielle and Abhijeet.

I would also like to thank UCLA staff for their tremendous support during my graduate student career. I am thankful for Mandy, Deeona and Michelle for guiding me through the typical trials and tribulations of graduate school with a sunny enthusiasm. I am grateful to Gershwin, Jose and Mac for their facilities support. I would also like to thank Marty and Laura for grant administration and purchasing support. I would like to also like to thank the CNSI/Nanolab

cleanroom staff, Brian (for help with wire bonding), Lorna, Da, Eve, Tony, Yuwei (ebeam patterning), Wilson, Joe, Max and Noah (for help with TEM prep).

I would like to thank my collaborators Prof. Yuhrenn Wu of National Taiwan University, Prof. Majeed Hayat and Dr. David Ramirez of University of New Mexico, Dr. Marc Currie at Naval Research Lab for high speed measurements, Prof. John David at the University of Sheffield, Dr. Andrew Marshal at Lancaster University, Prof. Siddhartha Ghosh at University of Illinois at Chicago, Dr. Hans Bechtel at Lawrence Berkeley National Laboratory and Dr. Peter Catrysse at Stanford University.

Finally, I would like to thank my family (Ammi, Thathi and Akki) and my partner in crime Helena for their unwavering support and patience during my PhD - I could not have done this without you.

Vita

Education

University of California Los Angeles
M.S. Electrical Engineering, 2009
San Jose State University
B.S. Electrical Engineering, 2007

Selected Publications

Senanayake, P.; Lin, A.; Mariani, G.; Shapiro, J.; Tu, C.; Scofield, A. C.; Wong, P.-S.; Liang, B.; Huffaker, D. L. *Appl. Phys. Lett.* 2010, 97, (20), 203108-3.
Senanayake, P.; Hung, C.-H.; Shapiro, J.; Lin, A.; Liang, B.; Williams, B. S.; Huffaker, D. L. *Nano Lett.* 2011, 11, (12), 5279-5283.
Senanayake, P.; Hung, C.-H.; Shapiro, J.; Scofield, A.; Lin, A.; Williams, B. S.; Huffaker, D. L. *Opt. Express* 2012, 20, (23), 25489-25496.
Senanayake, P.; Hung, C.-H.; Farrell, A.; Ramirez, D. A.; Shapiro, J.; Li, C.-K.; Wu, Y.-R.; Hayat, M. M.; Huffaker, D. L. *Nano Lett.* 2012, 12, (12), 6448-6452.

Patent disclosures

Plasmonically Enhanced Electro-Optic Devices and Methods of Production. Huffaker, D. L.; Senanayake, P.; Hung, C.-H. PCT No,: 14/073,670
Plasmonically Enhanced Nanopillar Separate Absorption Multiplication Diodes Huffaker, D. L.; Senanayake, P.; Hung, C.-H.; Farrell, A. U.S. Provisional Patent Application No,: 61/911,371

1. Motivation

This thesis investigates the potential for impact ionization engineering (I^2E) in the nanoscale utilizing a three dimensional (3D) electric field confined within an array of III-V nanopillars. I^2E has been exploited in planar avalanche photodetectors with impressive reductions in the excess noise, due to the size of the multiplication region being on the order of the ionization path length of the carrier. This concept can be extended to 3D nanoscale multiplication regions (3D-NMR) where the injection of the photogenerated carrier can be specifically engineered to impact ionize with narrow probability distribution functions of the ionization path lengths. Nanoscale engineering of impact ionization can allow an unprecedented reduction in excess noise factors and improvements in gain bandwidth products. Figure 1 illustrates the expected improvement in avalanche statistics based on the proposed 3D-NOAAD). In a 3D-NOAAD, photogenerated carriers absorbed due to the Nanopillar Optical Antenna are precisely swept into the 3D-NMR where they impact ionize immediately due to sharp gradients of the electric fields. Due to the geometry of the 3D-NMR, the probability distribution of the ionization path length becomes narrower producing a less

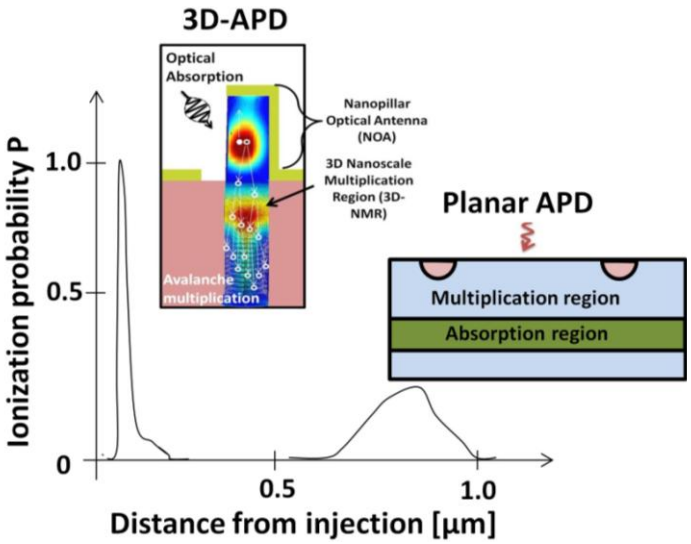

Figure 1: Comparison of engineering the avalanche statistics in 3D NMR compared to a planar APD

noisy avalanche gain. This is in contrast to a planar APD where a planar absorption and volume results in broader ionization path lengths.

1.1 Background on avalanche photodetectors

Avalanche photodetectors (APDs) are critical components for a wide range of technologies such as single photon detectors for quantum cryptography, high bit-rate telecom receivers, and active pixel elements for 3D LADAR imagers[1-3]. APDs absorb light generating a current, this current is internally amplified due a process called impact ionization. Typically, APDs are benchmarked in terms of their dark current, excess noise factor (F) and gain-bandwidth product[4]. The dark current is due to carriers other than photogenerated carriers being produced due to thermal generation, diffusion, and tunneling processes. Excess noise factor is the ratio of the measured noise spectral density to the multiplied shot noise[5] or can be understood as the fluctuations in the gain. Avalanche build-up time is the duration of the impulse response of an APD in the presence of gain and determines the limit of the gain-bandwidth product. These device parameters are critically dependent on the electric field engineered in the APD and the electron and hole ionization coefficients α and β respectively. McIntyre predicted that the excess noise factor can be related to the mean gain by[6] $F(M) = k_{eff}M + \left(2 - \frac{1}{M}\right)(1 - k_{eff})$, where $k_{eff} = \alpha / \beta$. McIntyre's result predicted that the excess noise depends only on the mean gain and k_{eff}, but not the size of the multiplication region. However, *shrinking the volume of the avalanche region*[2, 7-10] and engineering *sharp gradients in the electric field*[11] lowers k_{eff} resulting in lower excess noise factor and high gain-bandwidth products[4] beyond what is predicted by McIntyre's model. For impact ionization to take place a carrier must travel a certain distance

known as the dead space to gain sufficient energy from the electric field. Once the multiplication volume becomes on the order of the dead space length, k_{eff} is significantly reduced resulting in a lower F for a given M.

An additional benefit of a lower k_{eff} would be a higher gain-bandwidth products[4]. Emmons predicted the gain-bandwidth product achieved by APDs would be limited by the ratio of the electron and hole ionization coefficients. This is because the time required to remove the total charge generated from the avalanche process increases as the initial carrier produces more secondary carriers. The key point being that if an electron is initiating the avalanche process, secondary holes from the initial avalanche process could initiate further electron avalanches which add to the transit time delay. *In traditional planar APDs where the electric field is uniform in the plane parallel to the plane of epitaxy, and the i-region serves as the avalanche region for impact ionization, low values of* k_{eff} *usually comes at the cost of reduced ionization coefficients and higher breakdown voltages.* Novel multiplication region designs are necessary to overcome these traditional tradeoffs.

The improvements to APD performance mainly results from a more localized and coherent impact ionization process due to *reduced phonon scattering.* Once carriers are injected into the avalanche region it is favorable for them to ionize with a specific energy and distance. However, phonon scattering broadens the probability distribution of the ionization distance resulting in greater excess noise. Shrinking the volume of the avalanche region results in less collisions of these energetic carriers with phonons, producing a more coherent impact ionization process.

In a 3D-NOAAD there is unprecedented flexibility in engineering the avalanche statistics as the electric field distribution is not only determined by the 3D doping profile of the semiconductor nanostructure, but also its dielectric environment[12]. Further investigation of the fundamental physics of lower excess noise in nanoscale multiplication regions is necessary to understand the tradeoffs between lower k_{eff} and dark current due to tunneling.

1.2 State of the art APD technology

Silicon-based APDs have high QE in the visible, however their efficiency drops significantly in the near infrared (IR) wavelengths due to reduced absorption coefficient. Germanium is not suitable for IR APDs because they require cryogenic cooling (77K) to reduce the high dark current. Thus, InGaAs/InP APDs are the workhorse for near infrared photodetection with QE's of ~ 90% and excess noise factors of ~ 3 at a gain M =10[13-15].

Regarding application, the operating reverse bias in state-of-the-art InP-InGaAs APDs is typically in excess of 40 V. This value is just slightly less than the large breakdown voltage required to maintain acceptable levels of field-assisted dark carriers in the long multiplication region (>1.5 μm). Lowering the reverse bias to below ~ 15 V is desirable as it simplifies the bias circuits, especially in array configurations. To reduce the breakdown voltage in a planar APD requires the multiplication region to be below 500 nm. However, the required electric field to meet the breakdown condition increases field-assisted dark-carrier generation to unacceptable levels. Thus, wide multiplication layers (>1.5 μm) are preferred in planar APDs to minimize dark counts at the expense of the large reverse biases.

1.3 Active imaging and photon counting LADAR technology

One of the main application areas of 3D NOAADs are LADAR imagers, which allow the photon arrival times from objects to be determined allowing a 3D correlation of the object space 10 - 100 km away[5, 12]. Fig. 2(a) below shows a schematic of 3D imaging system[16] where a reflective

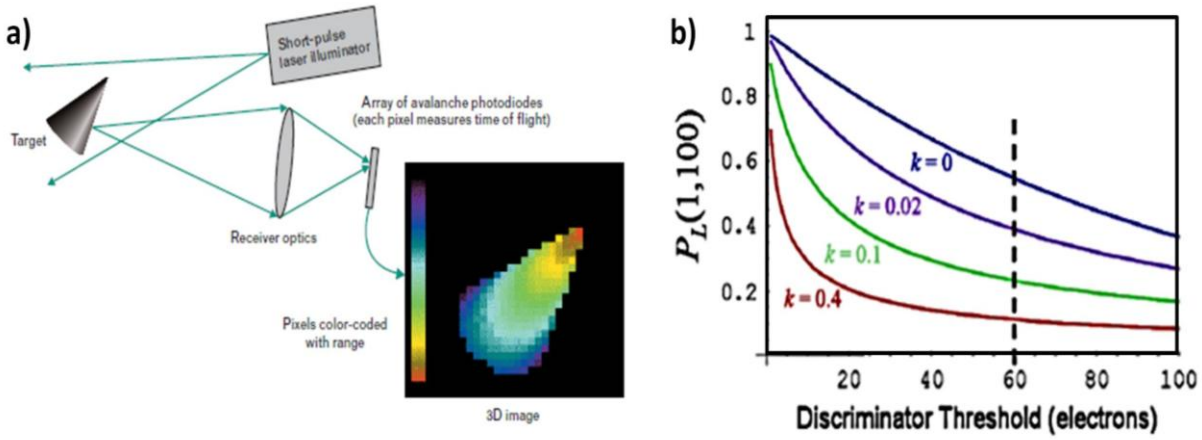

Figure 2: Schematic of 3D imaging system (taken from Albota et. al[16]) b) Probability of single photon detection vs. receiver noise threshold plotted for different values of k_{eff} (taken from Williams et. al.)[12]

cone is illuminated by pulsed laser illuminator. The reflected photons are detected are sensed by an array of single photon detectors where the time of flight instead of the intensity of photons allows the creation of a 3D image of the cone. The number of photons arriving at the APD array is extremely small such that the APD array requires sensitivity to single photon counting levels. In the case of a linear mode single photon detector, k_{eff} has a very large impact on the probability of detecting a single photon. From Fig. 2(b) it can be seen that the probability of detecting a single photon is ~ 60% given a keff ~ 0 and discrimator threshold of 60. Single carrier multiplication devices are therefore extremely useful for single photon detection with high detection probability.

A LADAR imager consists of APD arrays which are either operated in Geiger mode or linear mode. Geiger mode involves biasing the APD above its breakdown voltage such that the output current saturates while linear mode involves biasing the APD below the breakdown voltage such that output current is linearly proportional to the primary photocurrent. Geiger mode LADAR imagers have been preferred for single photon sensitivity, however they come at the cost of spurious detection events due to dark carriers. These spurious detection events slows down Geiger mode imagers limiting detailed 3D imaging. Linear mode operation on the other hand don't suffer from spurious detection events but needs to be implemented in concert with high performance amplifiers to reach single photon detection sensitivity.

LADAR imagers work on the principle of a pulse laser illuminator generating laser pulses which reflect off a target and are subsequently detected by the APDs. The returned pulses are imaged onto each pixel to form an image and sampled to obtained 3D information of the object. LADAR imagers based on Geiger mode APDs have been demonstrated[17]. The main problem with state of the art Geiger mode APDs is that single photon detection comes at the price of large dark currents and long deadtimes. *Sensitivity, speed and bandwidth requirements of the APD drive the design of LADAR imagers.*

1.4 Subwavelength metallic antennas coupled nanophotodiodes

Reduced quantum efficiency is a major challenge faced when scaling down the photodetector volume. A possible solution comes from the radio-frequency (RF) frequency range, where metallic antennas in receivers concentrate the electromagnetic field within a subwavelength volume. Researchers have explored different antenna configurations in coupling light into subwavelength absorption volumes. Rectangular gold nanorod antenna array on silicon

[18], circular metal hole arrays coupled to intersubband transitions in InAs QDs[19] and free standing metallic gratings integrated with HgCdTe photodetectors[20] exemplify the utilization of extra ordinary optical transmission (EOT) using near field optical field enhancements.

Indications that these concepts could be applied to the infrared and optical regime were further encouraged by observations of so-called "extraordinary optical transmission" of light through arrays of sub-wavelength holes in a metal film [21-27], or a single sub-wavelength aperture surrounded by a periodic bullseye pattern [28-31]. This phenomenon is accompanied by a significant enhancement of the electric field within the subwavelength aperture, which can be leveraged for a variety of photonic applications [25, 32, 33].

In general, the benefit of plasmonically-enhanced photodetection is that the "plasmonic antenna" [19, 34-38, 39] effectively collects light from a large area and concentrates it on a much smaller and thinner photodiode junction resulting in lower capacitance, and lower transit time. Various field enhancement mechanisms can be leveraged, including the enhancement near the metal/dielectric interface in a propagating Surface Plasmon Polariton Bloch wave (SPP-BW) [36, 40]. Also, resonant-field enhancement occurs in bounded metallic/dielectric structures that support Localized Surface Plasmon Resonances (LSPRs)[34, 35], such as metallic nanoparticles or nanoholes. These resonant field "focusing" mechanisms effectively increase the optical path length to be many times larger than the physical junction thickness. In principle, this allows the reduction of the detector volume even below the diffraction limit for more efficient integration, reduced leakage current for greater detector sensitivity, and reduction of the junction capacitance and transit time for higher speed detectors. Again, these demonstrations are planar (2D) configurations and based on complex lithographic techniques. We note that planar demonstration

of the plasmonic detectors fall substantially below theoretical predictions due to overlap of field intensity "hot-spots" with lossy metal. However, detectors operating in the near infrared (~1.55 μm) are spectrally close to the plasma resonances of noble metals and are expected to have large metal losses. This is not a concern in the case of the NOA due to the tight focusing of light within the semiconductor nanopillar instead of the lossy metal.[41]

1.4 Promise of proposed 3D-NOAADs - relaxing the QE vs. dark current tradeoff

In comparison to planar APDs, the structure and electric-field distribution of the 3D-APD have several key advantages with regards to impact ionization and APD sensitivity enhancement. The most important figure of merit to be improved in an APD is the detectivity which quantifies the improvement in sensitivity as defined in Equation 1 as[42]

$$D^* = \frac{\lambda\eta}{2hc\left(G(T)t\right)^{\frac{1}{2}}}\left(\frac{A_o}{A_e}\right)^{\frac{1}{2}} \qquad (1)$$

where h is the Plank constant, c is the speed of light, λ is the wavelength of light, η in the quantum efficiency, A_o is the optical collection area, A_e is the electrical area of the photodetector absorber, t is the thickness of the photodetector absorber, $G(T)$ is the thermal generation rate. From equation 1 it can be seen that the specific detectivity of the photodetector can be improved by *1) decoupling the optical collection from the electrical area such that* $A_o >> A_e$ *and 2) decreasing the volume of the photodetector absorption material such that the due generation noise* $\left(Gt\right)^{\frac{1}{2}}$ *can be reduced*. The 3D-NOAD focuses light from a large collection area (A_o) to a small absorbing foot-print (A_e) within the nanopillar enabling high QE. The small

footprint enables nanoscale engineering of the impact ionization process for improved APD figures of merit.

2.0 Nanopillar Optical Antenna for efficient wavelength tunable absorption

The NOA is the crucial technology enabling footprint reduction of the 3D-NMR, while maintaining high quantum efficiency. The NOA is a 3D plasmonic antenna structure which collects electromagnetic energy and concentrates it in a subwavelength area by coupling with surface plasmon waves[21-27, 43]. In the optical frequency range where the dielectric function of metals take on the plasma form these surface waves are known as Surface Plasmon Polaritons Bloch Wave (SPP-BW)[21, 44] or Localized Surface Plasmon Resonances (LSPRs). SPP-BWs have in-plane momentum, and therefore needs to be phase-matched by a

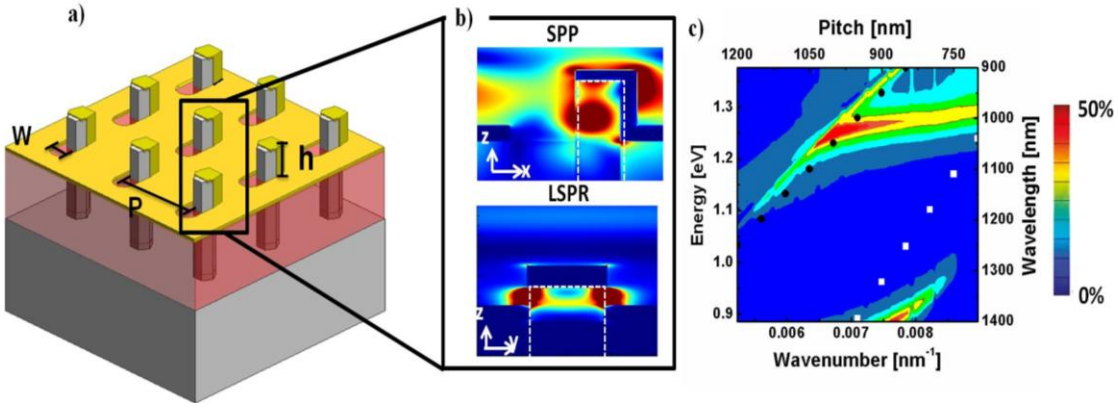

Figure 3: a) The Nanopillar Optical Antenna allows the coupling of both SPPs and LSPRs via geometry partial metal shell and self aligned metal nanohole b) Calculated external quantum efficiency of the NOA as a function of pitch of the self-aligned nanohole lattice

periodic surface corrugation to couple to normally incident light. LSPRs are supported by the specific shape of the metallic nanostructure[22, 45] and can directly couple to normally incident light. This thesis will demonstrate that the NOA can utilize both SPP-BWs and LSPRs for harvesting light for enhanced absorption within the nanopillar[41, 46].

The NOA consists of a partial gold shell on the nanopillar sidewalls and gold cap on top of the nanopillar along with a self aligned nanohole as shown in Fig. 3(a). The width of the nanopillar (w) and height (h) allows the focussing of LSPRs while the periodicity (P) of self aligned nanohole allows focussing of SPP-BWs within the nanopillar as shown in Fig. 3(b). The optical field enhancement due to the NOA takes place in the nanopillar instead of the lossy metal (as shown in Fig. 3(b)), which is the key enabling technology for nanoscale footprint and high quantum efficiency of the 3D-NOAAD. The geometry of the

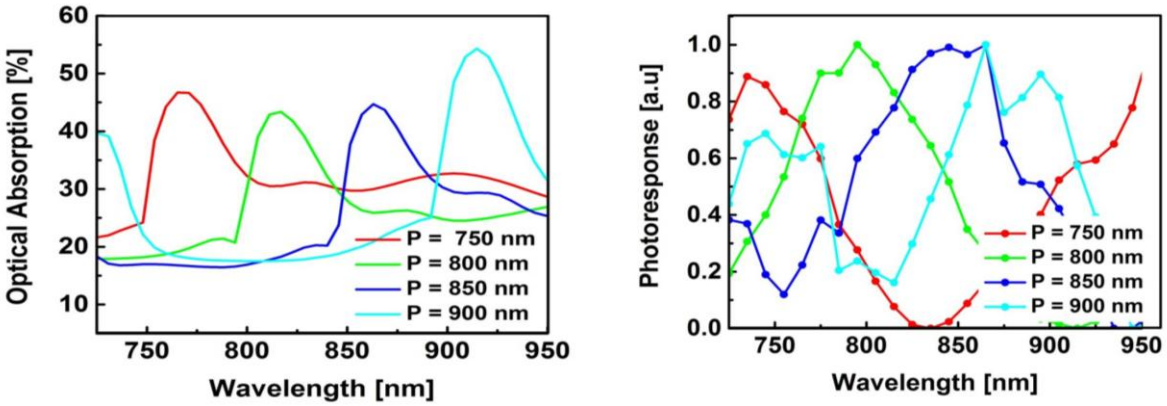

Figure 4: a) FDTD simulations of the power absorption spectra b) Measured photoresponse spectra

NOA can be tuned for high external quantum efficiencies at 1 μm. Figure 3(c) shows a contour map of the quantum efficiency of the NOA as a function of periodicity (P) while w and h are fixed. The NPs consist of $In_{0.35}Ga_{0.47}As$ with a diameter of 225 nm, and 550 nm in height arranged in square lattice. The dotted white and black lines corresponds to first order and second order SPP-BWs. In addition there is a third mode around λ = 1 μm which is independent of pitch, this is a LSPR excited due to the width and height of the nanopillar.

Due to the hybridization of the second order SPP-BW mode and LSPR a peak quantum of ~ 50% is achieved. ***These initial calculations indicate that the NOA can produce an external quantum efficiency in excess of ~50% shown in Fig. 4(a) at 1 μm.*** Increasing the pitch of the nanopillar results in the peak absorption of the resonances to shift as shown in Fig. 4(b). The ability to integrate tunable light

absorption using the NOA opens applications for hyperspectral imaging in SWIR and MWIR wavelengths.

Reflection spectroscopy of plasmonic antenna resonances

A key aspect of the electromagnetic design of the NOA structure is to critically couple incident radiation to the semiconductor nanopillars. In order to characterize optical absorption, simultaneous reflection/transmission measurements need to be performed. Typically reflection/transmission measurements are performed using unfocussed collimated light on large areas on the order of ~ cm^2. However, since NOA is manufactured using electron beam lithography it is not feasible to produce NOA arrays in a large cm^2 area.

The most significant challenge in measuring optical absorption is focusing the excitation light to the NOA patterned area on the order of 50 µm x 50 µm. Tightly focusing incident light using high numerical aperture (NA) objectives generates light with a range of incident angles. For example, typical Swazichild reflective objectives with a NA of 0.65 have incident angles ranging from 17^o - 42^o broadening plasmonic absorption features. Despite the broadening of plasmonic resonances, focused reflection measurements offer the highest spatial resolution characterization limited by the spot size[47] of the source or aperture size of the microscope[48].

In the Short Wave Infrared (SWIR) there are two schemes for focused reflection characterization: 1) A Fourier transform infrared (FTIR) spectrometer (Thermo Scientific 8700) integrated with an IR microscope (Thermo Scientific continuum) and a 2) fiber coupled spectrometer with NIR objective such as filmetrics F20-EXR. In both cases a white light source allows spectral measurements in the near infrared (NIR). The main distinction between the two systems is that the fiber coupled filmetrics system is limited to reflection measurements, while the Thermo Scientific system can measure both reflection and transmission from 1 - 10 µm wavelengths. While measurements of absorption will give information only about coupling to SPP-BW and LSPR modes regardless of their coupling to the semiconductor nanopillar,

simultaneous measurement and comparison of the photocurrent spectrum will provide a method to identify which SPP-BW modes of the plasmonic crystal result in the maximum photogeneration within the nanopillar. Fig. 5(a) and (b) shows a schematic of the FTIR/IR microscope configured in the reflection

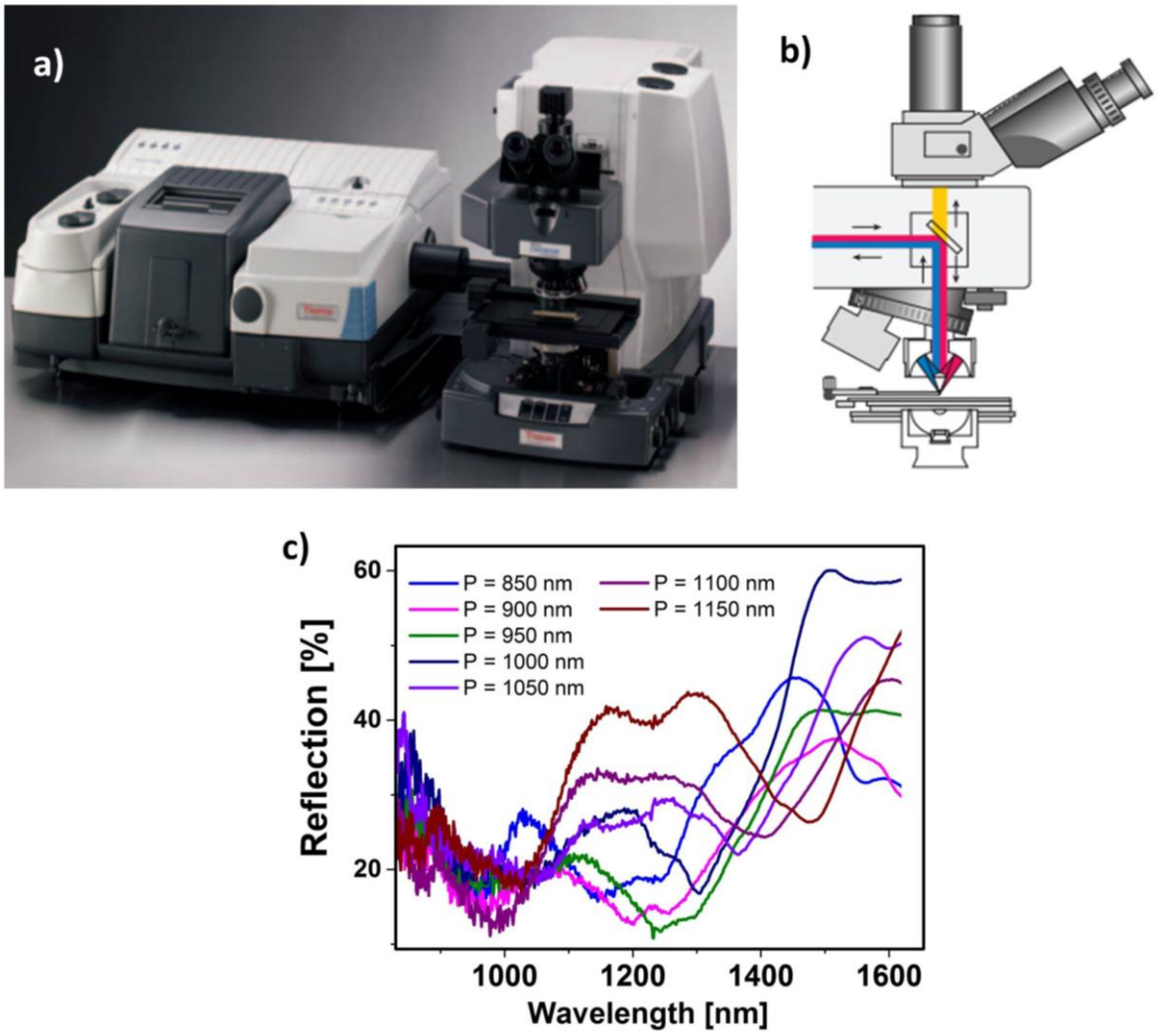

Figure 5: a) Nicolet 8700 FTIR pectrometer combined with continuum IR microscope b) Reflection mode configuration of continuum IR microscope (taken from Thermo Scientific brochure)[49] b) Reflection measurement of NOA array

mode for focused measurements[49]. Light from the white light source is focused onto the sample using one half of the aperture and the reflected light is collected and sent back to the spectrometer for spectral analysis. The spot can be observed via the beam splitter on the sample. Reflectance measurements were

performed on the NOA arrays as shown in Fig. 5(c). Both SPP-BW and LSPRs can be observed as reflection dips. The LSPR remains at fixed spectral position of ~ 1000 nm as the pitch is increased while the reflection dip due to the SPP-BW mode shifts by ~ 50 nm.

Electromagnetic simulations of surface plasmon resonances in nanopillars

To design the optical absorption in Nanopillar Optical Antenna Avalanche Detectors full wave finite difference time domain (FDTD) simulations are carried out using the commercial software Lumerical. The incident plane wave is polarized in both the x- and y- polarizations over

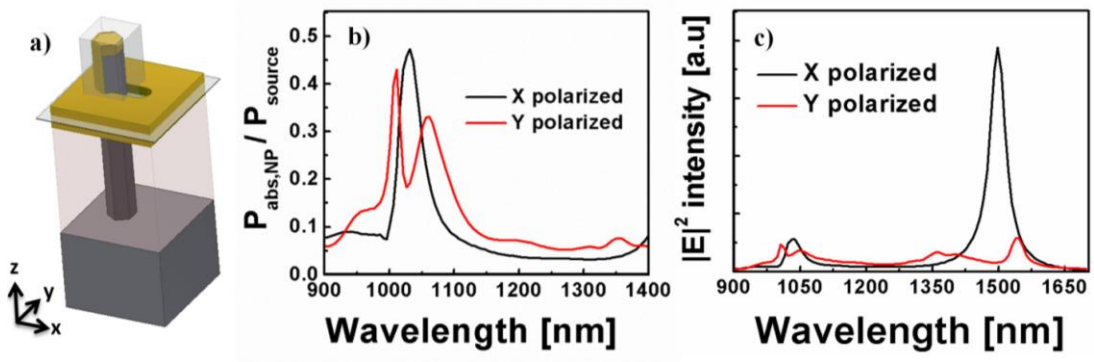

Figure 6: Structure definition for 3D FDTD simulation. b) FDTD simulation of the b) power absorbed in the x- and y- polarizations, and c) Electric field intensity.

a wavelength range of 900 – 1600 nm. The 3D unit cell of the modeled structure is shown in Fig. 6(a). Periodic boundary conditions are implemented in the x- and y- boundaries with a pitch of 1 μm. Perfectly Matched Layer (PML) boundary conditions are implemented in the z- directions. $In_{0.4}Ga_{0.6}As$ optical parameters[50] are used to describe the NP, GaAs optical parameters[51] are used for the substrate. A fine mesh of 1 nm x 1 nm x 2 nm is used in the gold and the tip of the exposed nanopillar in contact with the gold.

The fractional power absorbed in the nanopillar is computed by numerically evaluating Equation (2), where $\varepsilon''(\omega)$ is the imaginary part of the dielectric constant of $In_{0.4}Ga_{0.6}As$, and

$\left|E\left(\omega,x,y,z\right)\right|^2$ is the electric field intensity. The integral is evaluated within the volume of the $In_{0.4}Ga_{0.6}As$ nanopillar.

$$P_{abs}\left(\omega\right)=\iiint_{NP}\frac{1}{2}\omega\left|E\left(\omega,x,y,z\right)\right|^2\varepsilon''\left(\omega\right)dV \qquad (2)$$

Figure 6(b) shows the spectra for the fractional power absorbed in the NP for the x- and y- polarizations respectively. For the x- polarization there is a peak at 1030 nm where 47% of the incident light is absorbed in the nanopillar, while for the y- polarization there are two peaks at 1010 nm and 1060 nm. The peaks at 1030 nm for the x-polarization and 1010 for the y-polarization are attributed to $SP_{(\pm1,\pm1)}$ mode. The $SP_{(\pm1,\pm1)}$ mode is excited in both the x- and y-polarizations, where it is stronger in the x- than the y- polarization.

Figure 6(c) shows the spectra for the electric field intensity integrated over the NP volume for the x- and y- polarizations respectively. Mirroring the calculated power absorption spectrum in Fig. 6(b), the $SP_{(\pm1,\pm1)}$ are be observed in the integrated electric field intensity for both the x- and y- polarizations. In addition the x- polarization has an even stronger resonance at 1500 nm which is attributed to the $SP_{(0,\pm1)}$ resonance, which is largely absent for the y-polarization. However, this peak is not observed in the absorption spectra, as it lies at a longer wavelength than the cut-off of the InGaAs NPs at 1450nm. The strong $SP_{(0,\pm1)}$ resonance is very encouraging for future 1.55 μm device demonstrations since greater optical coupling efficiency of the $SP_{(0,\pm1)}$ mode into the NP would result in a much higher responsivity.

3. Fabrication of Nanopillar Optical Antenna Avalanche Detectors

For the devices studied in this dissertation, Zn-doped $In_{0.4}Ga_{0.6}As$ NPs are grown by selective-area epitaxy (SAE) on n+ doped GaAs (111) B substrates at 10^{18} cm^{-3} [52]. Figure 7a) shows a typical NP array before processing, and Fig. 7(b) shows an SEM image of the fully processed photodiode array. A schematic of the final device is shown in Fig. 7(c). The NPs have

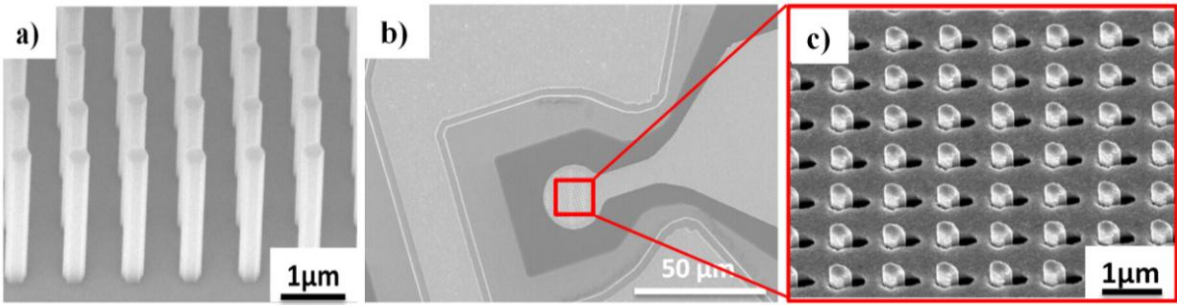

Figure 7: a) $In_{0.4}Ga_{0.6}As$ NPs grown on n+ GaAs by selective area MOCVD arranged in a square lattice with a 1µm pitch. b) Final fabricated APD showing high speed contacts c) Close up view of the nanopillar array showing the signal contact aligned to the nanopillar array.

a height of 1.3 µm, a diameter of 200 nm, and are arranged in a 1 µm pitch square lattice. The NP doping concentration is estimated to be $5x10^{17}$ cm^{-3} from single pillar resistivity measurements. A more detailed description of substrate patterning and NP epitaxy are published elsewhere[52].

Following epitaxy, the NP array is planarized using Benzocyclobutene (BCB), which is hard-cured and etched back to expose ~500 nm of the NP tips. The top metal contact (Cr: 20 nm, Au: 200 nm) is evaporated at 35 ^{o} from the substrate normal to coat both top and the exposed side of each NP along with the entire surface interconnecting the pillars. The NP "shadow" leaves the other pillar side uncoated and forms a self-aligned nanohole adjacent to each NP. The nanohole length depends on the exposed tip length and the incident angle of metal deposition,

while the nanohole width is defined by the NP diameter. The resulting nanoholes are 260 nm wide and 315 nm long. This metal nanohole array forms a 3D Nanopillar Optical Antenna self aligned to the NPs described in Section 2.

3.1 Polarization effects of plasmonically enhanced nanopillar photodetectors

Effects of the asymmetric self-aligned nanohole are elucidated through polarization-specific spectral response of the NOAAD described in Fig. 8 (a)-(c). As shown in Fig. 8a) the polarization of light with respect to the long axis of the nanohole is considered x-polarized and the polarization orientation is delineated using angle ϕ.

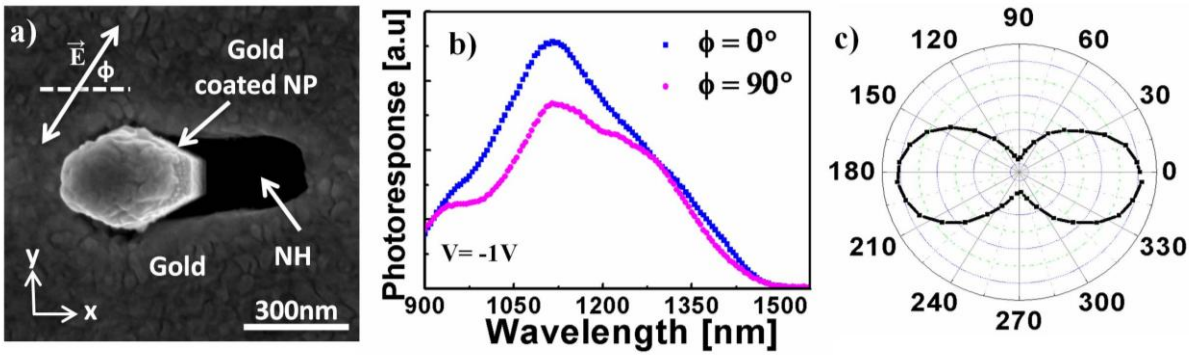

Figure 8:a) High resolution SEM of the nanopillar in the nanohole and orientation of the light polarization b) Photoresponse for x- and y- polarized light c) Polarization dependent photocurrent at 1100 nm showing $\cos^2(\varphi)$

As shown in Fig. 8(b) the photoresponse of the device when incident light is x-polarized light (ϕ = 0 ˚) produces a higher photocurrent compared to the y-polarized light (ϕ = 90 ˚) for much of the photoresponse spectrum, except at 1260 nm where the photocurrent for both polarizations is the same. It is interesting to note that the peak responsivity for both ϕ = 0 ˚ and ϕ = 90 ˚ occur at 1110 nm independent of polarization suggesting photoresponse enhancement due

to $SP_{(\pm1,\pm1)}$ mode. Fig. 8(c) shows a polar plot of the photocurrent for incident wavelength at 1100 nm. The photocurrent is measured at the peak responsivity of λ = 1100 nm from $\phi = 0^{\circ}$ through a full 360 ^{o} revolution at 10 ^{o} increments. The maximum photocurrent is measured for the x-polarization with a 25% drop in the photocurrent for y-polarized light. The photocurrent shows a $\cos^2\phi$ dependence on the incident light polarization similar to the optical antenna behavior observed with gold nanorods[53]. In the case of the control device there is no dependence of the photoresponse on polarization. This dipole-like dependence of the photocurrent is commonly attributed to the specific nature of the Localized Surface Plasmon (LSP) that is excited in the gold nanohole[22, 44, 53]. However, the polarization dependence of the spectral response is the opposite expected of an elongated nanohole, where the maximum transmission occurs at $\phi = 90^{\circ}$ and the minimum at $\phi = 0^{\circ}$.

Localized Surface Plasmon Absorption

The NOA is advantageous for improving the signal to noise ratio of nanopillar photodetectors because it allows optical absorption greater than geometrical cross-section of the nanopillar. Fig. 9(a) shows a schematic of a single NOA which consists of a nanopillar with width ***w***, exposed nanopillar height of ***h***, and the partial gold shell. Specifically, ***h*** is the height of the nanopillar above the polymer (bisbenzocyclobutene - BCB) planarization layer. LSPRs can be spectrally tuned by varying the geometry of the (NOA) in terms of ***w*** and ***h***. The NOA supports LSPRs due to the metal cap on top of the nanopillar, and the metal shell on the sidewalls of the nanopillar. The absorption of a single NOA is studied by full wave FDTD simulations using the total field scattered field approach. In the TFSF approach the boundary

conditions are Perfectly Matched Layer (PML) boundary conditions in the x- y- and z-boundaries, and the illumination is replaced with a total field/scattered field source, which isolates the scattered light outside the source [54, 55].

The optical properties of gold in the near infrared was modeled using Johnson and Christy [56]. Light is normally incident and polarized along the long edge (x-direction) of the nanohole, such that it is more efficiently absorbed as reported previously [56]. The total electric field intensity enhancement inside the nanopillar is quantified using the normalized absorption cross-section ($\boldsymbol{Q_{abs}}$), which is defined as the absorption cross-section normalized to the cross-section of the nanopillar as shown in Eq. (3). The parameters of Eq. (3) are ω which is the

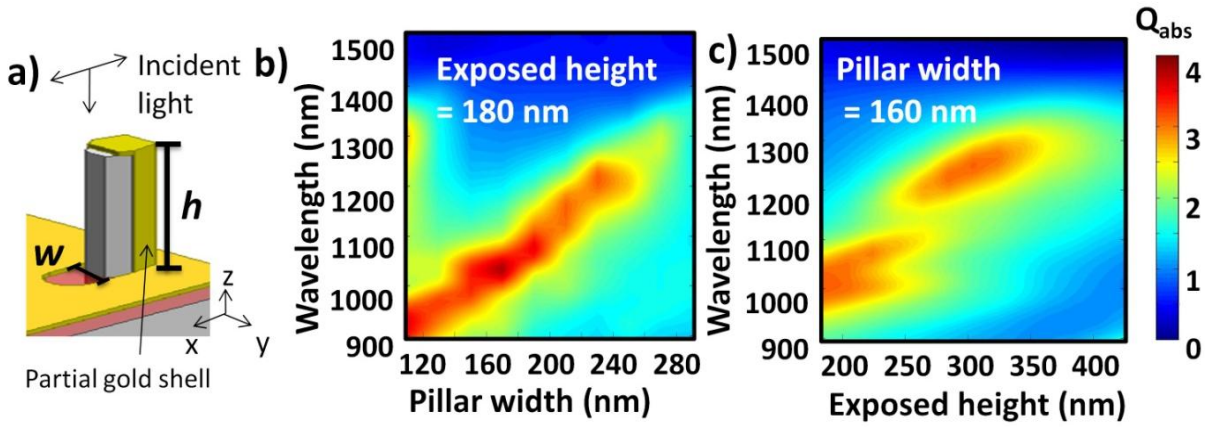

Figure 9: a) Schematic of Nanopillar Optical Antenna (NOA). Contour plot of the Q_{abs} as b) w is varied, and c) as h is

angular optical frequency, ε'' is the imaginary part of the dielectric permittivity of $In_{0.3}Ga_{0.7}As$[50], $\left|\vec{E}\right|^2$ is the electric field intensity inside the nanopillar, I_{source} the intensity of the total field scattered field source, and A_{NP} the cross-section area of the hexagonal nanopillar [54]. $\boldsymbol{Q_{abs}}$ is a measure of the funneling of light from a larger collection area and absorption into the nanopillar.

$$Q_{abs} = \frac{\iiint_{NP} \frac{1}{2}\omega\varepsilon''\left|\vec{E}\right|^2 dV}{I_{source}A_{NP}} \qquad (3)$$

Fig. 9(b) and (c) show contour plots of $\boldsymbol{Q_{abs}}$ as the geometry of the NOA is varied. In Fig. 1(b) $\boldsymbol{h}$ is kept constant at 180nm, and the width of the nanopillar is varied. The peak value of $\boldsymbol{Q_{abs}}$ smoothly shifts to longer wavelengths with increasing width such that a maximum value of ~3.9 is

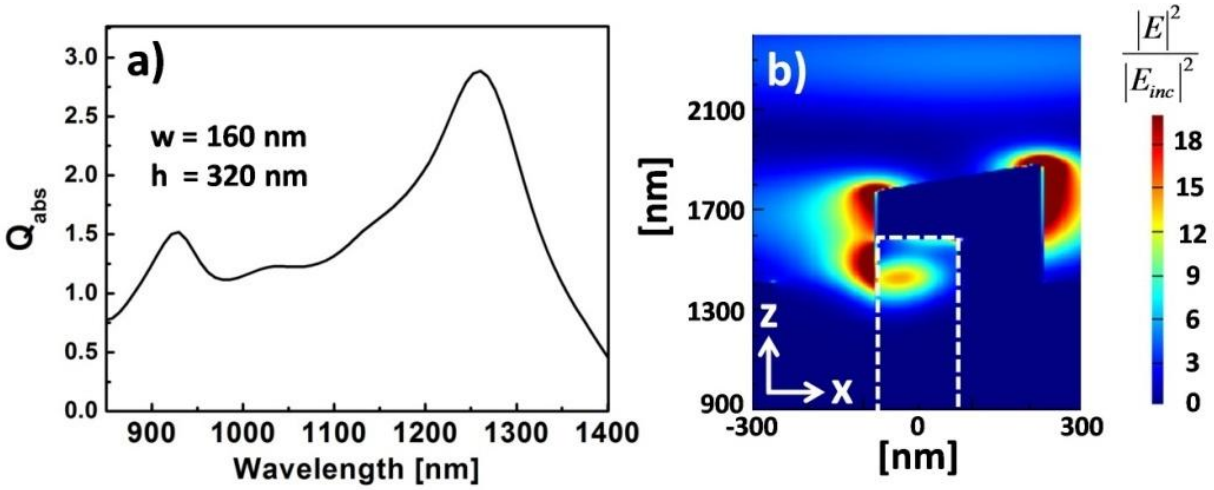

Figure 10: a) Absorption enhancement due to the Localized Surface Plasmon (LSPR) supported by the metal cap b) Electric field intensity profile of LSPR mode at 1270 nm in x-z plane

obtained for a width of ~ 160 nm. In Fig. 9(c) $\boldsymbol{w}$ is kept constant at 160 nm, and the exposed height $\boldsymbol{h}$ is varied. The peak value of $\boldsymbol{Q_{abs}}$ in this case also shifts to longer wavelength as the exposed height increases, however there are two hot spots in the absorption cross-section. The first hot spot in the $\boldsymbol{h}$ = 200 - 250 nm range is due to an LSPR supported mainly by the metal cap. The second hot spot in the $\boldsymbol{h}$ = 300 - 350 nm is due to an LSPR supported mainly the partial metal shell. These simulations show that the NOA supports LSPRs, and that the optical absorption can be tuned by the three dimensional geometry of both the nanopillar gold cap and partial gold shell covering the nanopillar.

The highest enhancement in $\boldsymbol{Q_{abs}}$ is obtained when $\boldsymbol{h}$ is equal to the thickness of gold on polymer planarization such that $\boldsymbol{w}$ = 160 nm and $\boldsymbol{h}$ = 180nm.

A representative spectrum of the enhancement of $\boldsymbol{Q_{abs}}$ is shown in Fig. 10(a). The NOA geometry is such that $\boldsymbol{w}$ = 160 nm and $\boldsymbol{h}$ = 320 nm. The peak value of $\boldsymbol{Q_{abs}}$ is ~ 2.8, while the peak absorption takes place at 1270 nm. This geometry of the NOA was chosen such that the LSPR could be clearly distinguished from the SPP-BW modes. Fig. 10(b) shows the electric field intensity in the x-z plane. The nanopillar is outline by a dotted white line. Electric field enhancements within the nanopillar can result in useful photogeneration and enhanced photocurrent. The electric field extends from the metal cap on top of the nanopillar down to the nanopillar where it is absorbed. The LSPR due to the metal cap can be tuned by varying the exposed height of the nanopillar. At its peak value, the electric field intensity inside the nanopillar is x10 the incident electric field intensity. The LSPR forms a vertical dipole resonance from the metal cap on top of the nanopillar and the partial metal shell on the nanopillar sidewalls. This kind of LSPR is qualitatively similar to nanopatch antenna structure used for plasmonic lasers except the case of the NOA has a broken ground plane [57].

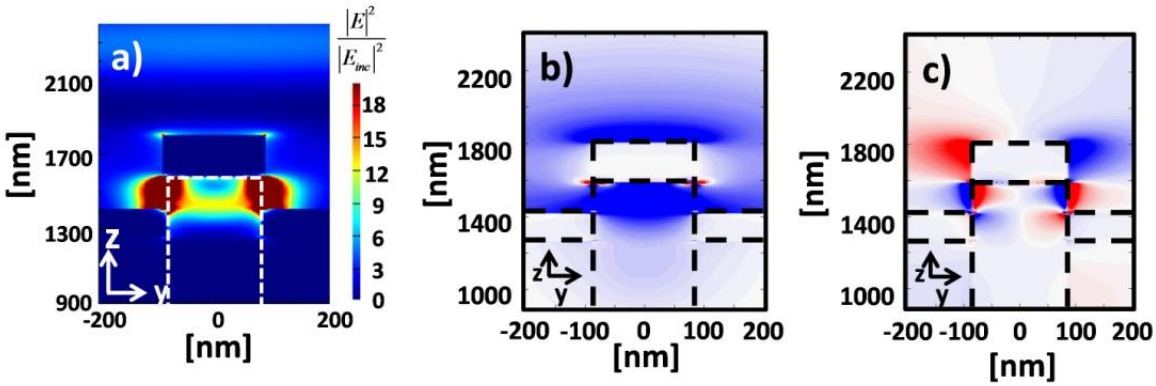

Figure 11: . a) Electric field intensity in the y-z plane of the LSPR mode at 1270 nm and the corresponding electric field in b) the z-direction E_z and c) y-direction E_y

The nature of the LSPR due to the partial gold shell can be further investigated by decomposing the electric field intensity into its constituent field components. Fig. 11(a) shows the electric field intensity of the NOA structure in the y-z plane. The electric field intensity enhancement is greatest near the partial gold shell on the nanopillar sidewalls (greater than x18 the incident electric field intensity), and lowers towards the center of the nanopillar. Fig. 11(b) shows the electric field component in the z-direction (E_z). E_z is pointing downwards in the nanopillar and maximum in the center of the nanopillar . Fig. 11(c) shows the electric field component in the y-direction. The direction of E_y changes on the side walls of the nanopillar due to the partial metal shell coating the sidewalls. These results indicate that the enhancement in electric field intensity of the NOA is due to LSPRs of the metal cap on the nanopillar producing enhancement in the z-directed electric field and the partial metal shell on the sidewalls of the nanopillar producing an enhancement in the y-directed electric field.

Angular spectral response mapping of plasmonic absorption

Fig. 12 shows the experimental angle-dependent photoresponse at zero bias. For the photoresponse characterization the photocurrent of the wire bonded device is measured using a Keithley 2402 multimeter. Light from a quartz halogen lamp is dispersed by a grating monochromator and is incident on the device. In order to characterize the plasmonically enhanced absorption, photocurrent contributions from the different plasmonic modes need to be identified and quantified. SPP modes have a characteristic dispersion related to its propagation in the plasmonic crystal. This dispersion can be measured using variable angle photocurrent spectroscopy, as illustrated in Figure 12(a) [19, 41, 58, 59]. This measurement can be used to quantify

what proportion of incident radiation is coupling to SPP modes and map these modes by varying

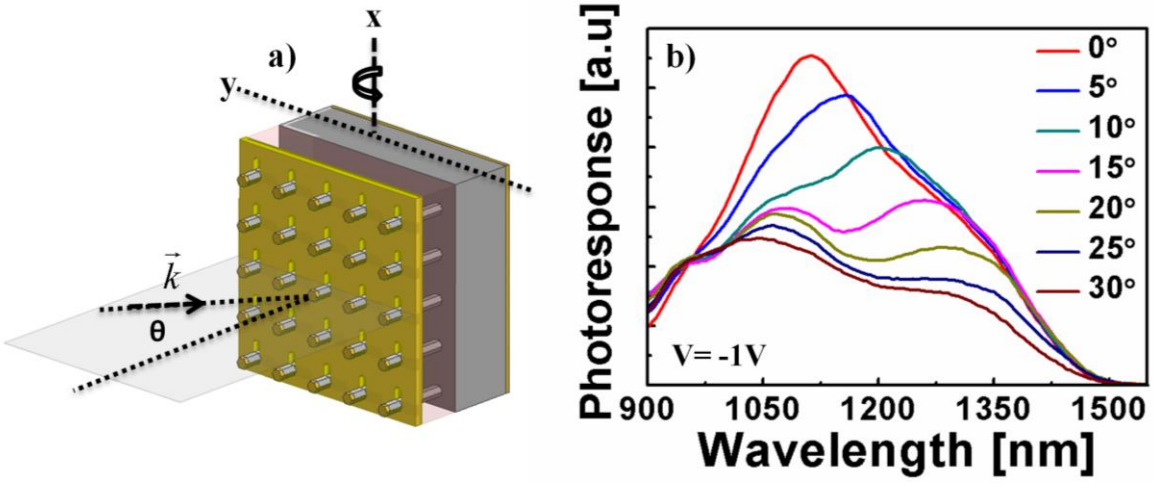

Figure 12: a) Schematic of the sample orientation in the angle dependent photoresponse measurement. b) Angular photoresponse of the gold nanohole array photodetector showing the shift and splitting of the $SP_{1,1}$ resonance.

the angle of incidence. A quartz-tungsten halogen lamp is used as the illumination source in a variable angle photocurrent spectroscopy setup that allows measurements spanning incident angles from 0-80º. Typical angular photoresponse spectra of plasmonically enhanced nanopillar detector is shown in Figure 12(b). Specifically, Figure 12(b) shows that the peak responsivity occurs at ~1110 nm is roughly described by the (1,1) scattering order of the SPP mode[58].

$SP_{(\pm1,\pm1)}$ degenerate modes will split into the $SP_{\pm1,-1}$ and $SP_{\pm1,+1}$ modes with increasing incident angle θ. At normal incidence (θ = 0) the $SP_{\pm1,\pm1}$ modes are degenerate, resulting in the peak at 1112 nm. As θ is increased the photoresponse peak at 1112 nm red shifts due to the $SP_{\pm1,-1}$ modes, and also broadens due to the $SP_{\pm1,+1}$ modes. Eventually at $\theta \geq 15^{o}$, the single peak has clearly split into two peaks in good qualitative agreement with the interpretation of the photoresponse shift as being due to SPP field enhancement in the nanopillars.[41]

2.1 Hybridizing LSPRs and SPP-BWs

NOAs can be arranged in a lattice such that the optical absorption can be further enhanced by the overlap of SPP-BWs [56] and LSPRs resulting in hybridized plasmonic modes for enhanced photoresponse. The boundary conditions of the simulation are changed to periodic boundaries in the x- y- directions, while the incident illumination is a plane wave source. The nanopillar exposed height and nanopillar width are chosen to be ***h*** = 320 nm and ***w*** = 160 nm to couple LSPRs due to the NOA structure described earlier. A pitch of 580 nm was chosen such that 1) the resonance of the SPP-BW can be clearly distinguished from the NOA resonance and

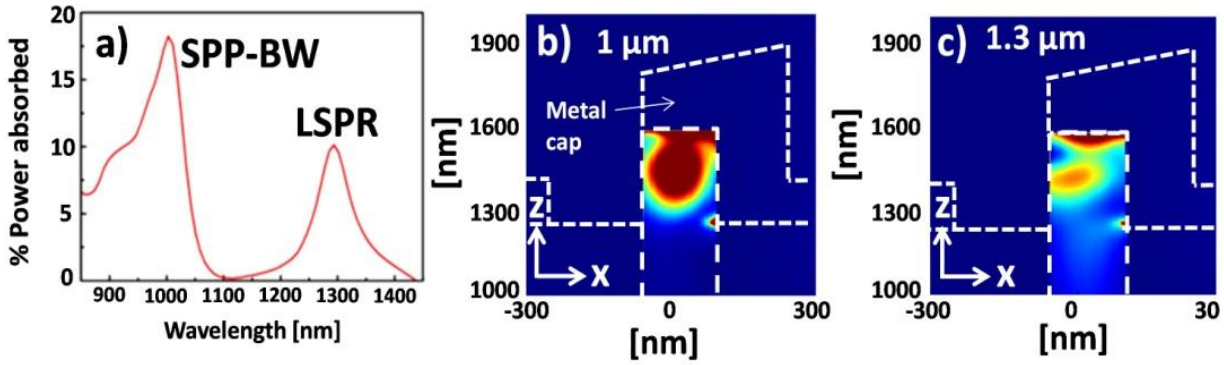

Figure 13: a) The full-wave simulation of the optical absorption in the nanopillar array for P = 580 nm. Power absorbed in the x-z plane for b) the SPP mode and c) LSPR mode.

2) resonances are within the absorption spectrum of the $In_{0.35}Ga_{0.65}As$ material.

Fig. 13(a) shows the fractional power absorbed in the nanopillar per unit cell. The first peak at 1000 nm is due to the SPP-BW mode, which is only appears when periodic boundary

conditions are used. While the second peak at 1300 nm is due to the LSPR, which is the same as is present in Fig. 10(a). Approximately 18% of the incident light is absorbed in the nanopillar due to the SPP-BW mode, while ~ 10% is absorbed due to the LSPR mode at 1295 nm. It should be noted that the absorption efficiency of the SPP-BW mode is not limited to 18% and can be further enhanced by optimizing the geometry of the self aligned nanohole lattice. Fig. 13(b) and Fig. 13(c) shows the power absorption profile of the SPP-BW and the LSPR modes excited in the structure at normal incidence. In the case of the SPP-BW mode, light is focused away from the metal into the nanopillar, and extends downwards from the gold on top of the nanopillar. In contrast the second peak at 1300 nm has an absorption profile very similar to the LSPR described in Fig. 10(b), which demonstrates that LSPRs supported by the NOA structure can be utilized for enhanced absorption in an array format.

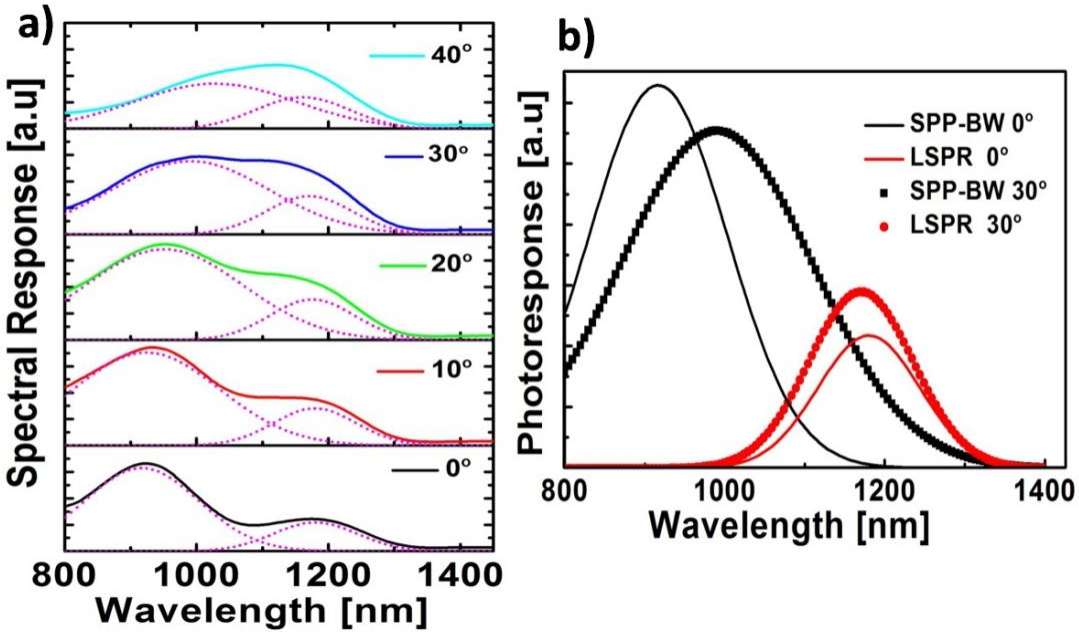

Figure 14: a) Measured angular photoresponse spectra of PENPD showing enhanced photocurrent due to both $SPP_{-1,0}$ and LSPR modes. P = 580 nm w = 160 nm h = 320 nm b) Fitting of the SPP-BW and LSPR before and after overlap at 0 °

Two peaks can be observed in the normal incidence photoresponse spectrum. The first peak at 923 nm is attributed to the SPP-BW$_{(0,1)}$ mode corresponding to the FDTD mode calculated at 1000 nm while the second peak measured at 1200 nm is attributed to the LSPR calculated at 1275 nm. For the angular photoresponse characterization the sample is mounted on a rotation stage described previously [56] and tilted with respect to the incident light. When the device is tilted (θ) with respect to normal, incident photons have an in plane momentum given by $k_{in-plane} = k_0 \sin(\theta)$ and the phase matching condition with surface plasmon polaritons is altered. Figure 14(a) shows that the photoresponse due to the SPP-BW mode red shifts from 915 nm at θ = 0 ^{o} to 990 nm at θ = 30 ^{o} and spectrally overlaps with LSPR at 1180 nm for maximum enhanced photoresponse. The peaks of the photoresponse spectra are fitted to Gaussian peaks to determine the peak position and line width of the SPP-BW mode and LSPR as shown in Fig. 14(b). A Gaussian fitting was chosen because the device consists of ~ 100,000 nanopillars such that the photocurrent measurement is an ensemble measurement. At zero bias θ = 0 ^{o} before the overlap of the SPP-BW and LSPR modes the responsivity at 1180 nm due to the LSPR is 0.048 A/W. Due to the overlap of the SPP-BW and LSPRs at θ = 30 ^{o} a responsivity of 0.096 A/W is measured at 1180 nm, which is a ~ x2 enhancement in the responsivity at LSPR wavelength due hybridization with the SPP-BW mode.

Plasmonic bandstructure

To further understand the coupling of the hybrid plasmonic modes excited, photonic bandstructure calculations were performed. The photonic band structure of the device is computed by the fast fourier transform (FFT) of the time decay of the electric field intensity time

monitor in the nanopillar. An excitation dipole placed above the elongated hole with Bloch boundary conditions, and the in-plane momentum is varied in the y-direction. These simulations performed with periodic boundary conditions reveal several modes which did not previously appear in the simulations performed with PML boundary conditions (Fig. 10(a)) – we consider these to be SPP-BW modes supported by the gold/bcb interface and the gold/air interface. However, only the SPP-BW mode due to the gold/BCB interface results in useful optical absorption in the nanopillar.

Fig. 15(a) shows the FDTD simulated bandstructure of the device with **P** = 580 nm , **w** = 160 nm, and **h** = 320 nm. At the gamma point light couples predominantly into a band with a very

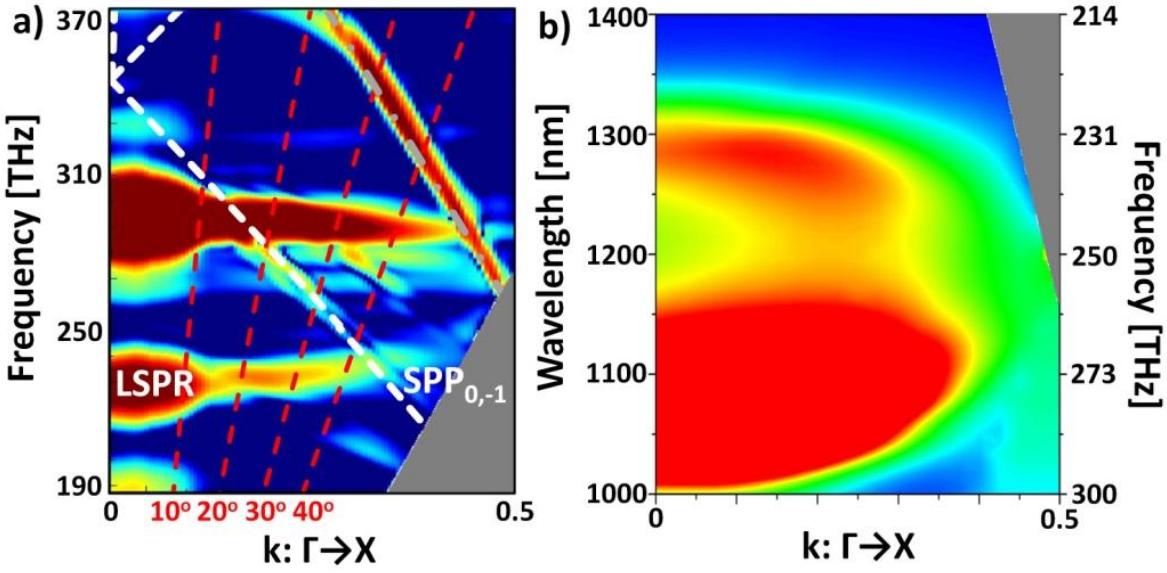

Figure 15: a) Simulated photonic bandstructure of NP-PEPD with P = 580 nm showing the SPP-BW Gold-BCB modes and Gold-Air modes. b) the absorbed power in the nanopillar.

low group velocity at 1000 nm (~310 THz) such that the light is efficiently absorbed in the nanopillar, which is ideal for vertically incident photodetectors [60]. There is also a secondary peak at ~ 1300 nm (~ 230 THz) due to the LSPR, which shows little dispersion with in plane

momentum characteristic of a localized resonance. Fig. 15(a) also shows the analytical SPP-BW dispersion of a gold hole array on polymer overlaid with the FDTD simulated bandstructure. The analytical expression for the dispersion of the SPP-BW modes is given by Eq. (4) [21, 61], where $\lambda_{SPP-BW_{i,j}}$ is the resonant scattering orders of the metal hole array, P is the pitch, ε_d is the dielectric constant of the polymer, ε_{Au} is the dielectric constant of the gold, and $k_{inplane}$ is the in-plane momentum in the direction perpendicular to long side of the hole. There are three white lines which denote the Gold/polymer SPP-BW modes.

$$\lambda_{SPP-BW_{i,j}} = \frac{2\pi\left(\frac{\varepsilon_d \varepsilon_{Au}}{\varepsilon_d + \varepsilon_{Au}}\right)}{\left(\left(\frac{2\pi}{P} i\right)^2 + \left(k_{inplane} \pm \frac{2\pi}{P} j\right)^2\right)^{\frac{1}{2}}} \qquad (4)$$

The $SPP_{(1,0)}$ and $SPP_{(-1,0)}$ modes at 344THz are degenerate at the gamma point and does not exhibit in-plane dispersion as these modes propagate in the x-direction. The $SPP_{(0,1)}$ mode is also at 344 THz at the gamma point and shifts to shorter wavelengths with increasing in plane momentum. However, the $SPP_{(0,-1)}$ mode shifts towards longer wavelength with increasing in plane momentum, and is the candidate SPP-BW mode for overlapping with the NOA resonance for enhanced photoresponse. Away from the gamma point the dispersion of the analytically computed $SPP_{(0,-1)}$ matches that of the numerically computed bandstructure as is seen in the dotted white line in Fig. 15(a). However this prediction fails close to the Gamma point ($\theta < 10$ degrees).

The dashed red lines in Fig. 15(a) correspond to the incident illumination being tilted an angle θ with respect to normal. From 0^o to 20^o the dispersion of the FDTD computed electric

field intensity at 301 THz does not considerably red-shift with in-plane momentum, and is possibly do to SPP-BW mode having a very low group velocity. However, beyond 20^o the SPP-BW red-shifts further such that at 30^o the SPP-BW has the greatest overlap with LSPR. The dispersion of the numerically computed bandstructure matches the analytical expression for the $SPP\text{-}BW_{(0,-1)}$ mode. Further increasing the incident angle results in the electric field intensity due to the $SPP_{(0,-1)}$ being much weaker in the nanopillar resulting in reduced photoresponse. The bandstructure calculations qualitatively corresponds to the angular photoresponse measurements shown in Fig. 14. Due to the low group velocity of the SPP-BW mode the photoresponse peak does not shift with in plane momentum upto a tilt of 20^o, beyond 20^o the SPP-BW red shifts. In addition to the Gold/BCB SPP-BW modes the structure also supports SPP-BW modes due to the Gold/Air interface shown as the dotted gray line, which has a good fit with the numerically computed FDTD bandstructure. However, these modes don't contribute to electric field intensity enhancement in the nanopillar resulting in useful photogeneration.

Fig. 15(b) shows the power absorbed in the nanopillar resulting in useful photoresponse. The SPP-BW mode from the gold/air interface (gray line in Fig. 15(a) doesn't contribute to useful photogeneration. However, the coupling of the SPP-BW (0,-1) from air/BCB interface and the LSP resonance results in enhanced photoresponse. The calculated power absorbed spectra in Fig. 15(b) supports the experimental result that a combination of $SPP\text{-}BW_{(0,-1)}$ and the LSP resonance is producing enhanced photoresponse. Hybridizing SPP-BW modes with LSPRs results in photoresponse spectra that is more broadband than the individual plasmon resonances.

3.0 GaAs homojunction 3D-NOAADs

Efficient carrier punch-through from the low field absorption region into the high field multiplication region is of paramount importance in the design of the 3D NOAADs.[62] Photogenerated carriers can recombine due to surface states of the nanopillar or trap states at the InGaAs-GaAs heterojunction limiting device efficiency. Three-dimensional finite element modeling of the nanopillar heterojunctions and its surfaces are a necessary component in

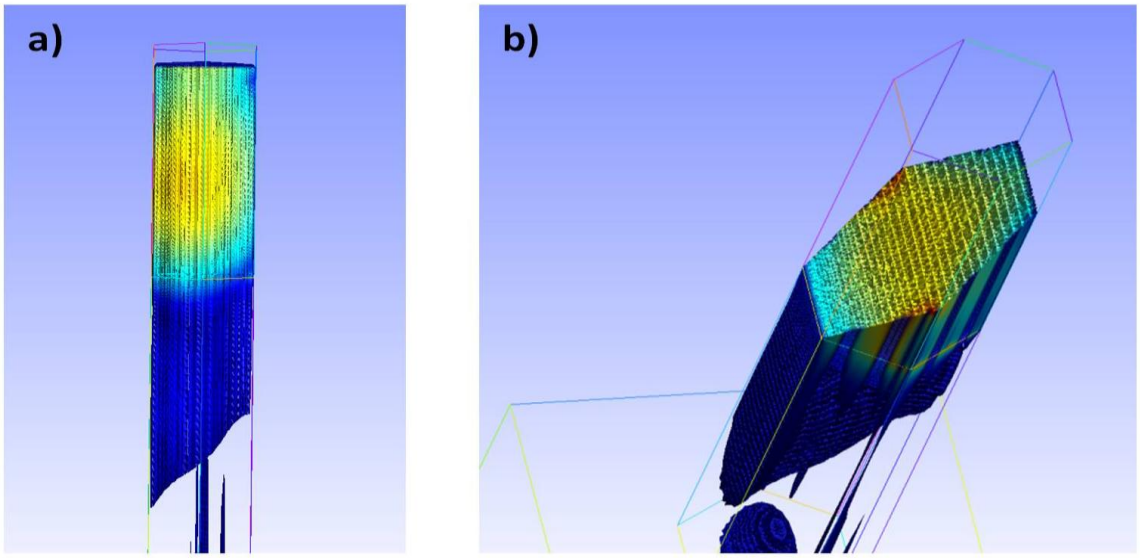

Figure 16: Plasmonically enhanced photogeneration rates in the low field GaAs absorber a) on the surface b) a cut through the nanopillar

nanostructure device design. Three-dimensional Drift-diffusion to model 3D NOAAD device characteristics, by solving the basic Poisson and drift-diffusion equations without simplification

in three dimensions and can be used for arbitrary device geometries. New physical models based on specific material properties of the nanopillar can be incorporated such as trap assisted recombination and tunneling. Figure 16(a) and (b) shows electron carrier density due to the plasmonically enhanced photogeneration. Carrier extraction might be reduced due to electron trapping at the InGaAs – GaAs heterojunction, we believe this can be overcome with a compositionally graded InGaAs absorption region reducing the band offset for carrier extraction. The 3D photogeneration rates computed by electromagnetic simulation will be imported into the 3D drift diffusion calculations to estimate bias dependent quantum efficiency of the 3D NOAAD. Models of dark current, trap densities and estimate carrier recombination at the surface will be extracted by fitting to temperature dependent dark current measurements to experimental results. The 3D electric field profiles generated by drift diffusion modelling will also used to model avalanche gain and excess noise of the 3D NOAADs.

3.1 GaAs core-shell nanopillar APDs

Figure 17(a) illustrates the structure of the NP APD comprised of a p-GaAs absorber (150

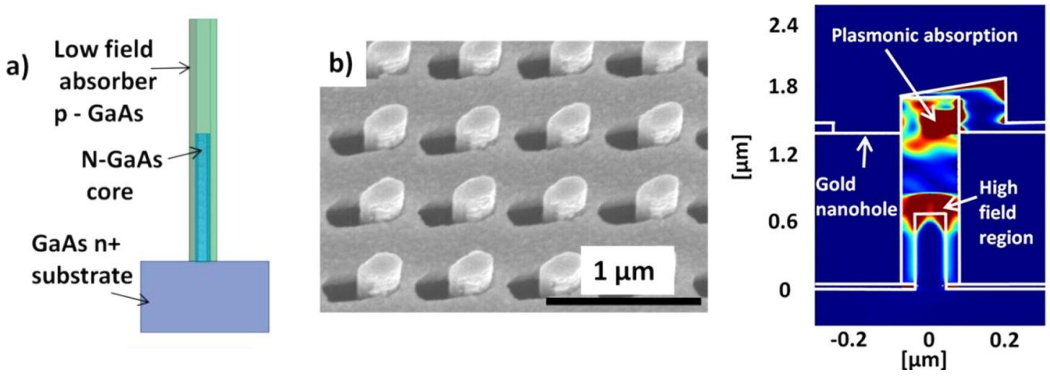

Figure 17: a) Schematic of the separate absorption multiplication avalanche diode. (b) Self-aligned metal nanohole lattice for plasmonically enhanced absorption. (c) Plasmonically enhanced photogeneration within the nanopillar.

nm in width and 900 nm in height) atop a core–shell GaAs PN junction.

The n-GaAs core is 80 nm in width and 800 nm in height, while the p-GaAs shell is 35 nm thick surrounding the core. The intended n-core and p-shell doping levels are both $\sim 10^{18}$ cm^{-3}. The nanopillars are encapsulated with an $In_{0.5}Ga_{0.5}P$ high bandgap passivation layer (not shown) to mitigate the effect of surface states[63]. Figure 17(b) shows a SEM image of the 3D self aligned plasmonic antenna for enhanced absorption within the GaAs nanopillar, engineered to take place within the GaAs bandgap at $\lambda \sim 730$ nm. Photogenerated electrons created within the tip of the nanopillar drift to the core-shell multiplication region with applied bias as shown in Fig. 17(c).

Figure 18(a) shows the typical light and dark current–voltage (*I–V*) characteristics of the nanopillar array contacting ~149160 NPs at 300 K. The dark *I–V* characteristic in Figure 18(a) can be fit to the ideal diode equation where the current, *I*, is given by $I = I_o \exp(q(V - IR_s)/nkT)$, I_o is the saturation current, R_s is the series resistance, *q* is the elementary charge, *T* is the temperature, *V* is the bias voltage, and ideality factor *n*. The nanopillar array devices exhibit excellent diode characteristics with a low series resistance of ~40 Ω, ideality factor of 1.6, and saturation current of 3×10^{-12} A. These diode characteristics suggest a high quality PN junction is formed within the nanopillar. At zero bias, under light conditions, an extremely low photocurrent of 20 nA is measured, indicating that a short diffusion length ($\ll$ 1 μm) results in the photogenerated carriers not being extracted by the core–shell electric field. However, as the reverse bias is increased, the photocurrent increases corresponding to both (1) an increase in the field dependent diffusion length of photogenerated carriers[64] and (2) an extension of the depletion region into the low field absorber. At −3 V, all of the photogenerated carriers in the

nanopillar are extracted, forming a plateau region in the photocurrent resulting in a responsivity of 0.27 A/W at 730 nm. This bias voltage corresponds to the punch through voltage indicating the maximum expansion of the depletion region. Further biasing the device results in the photocurrent being multiplied beyond the primary photocurrent due to avalanche multiplication.

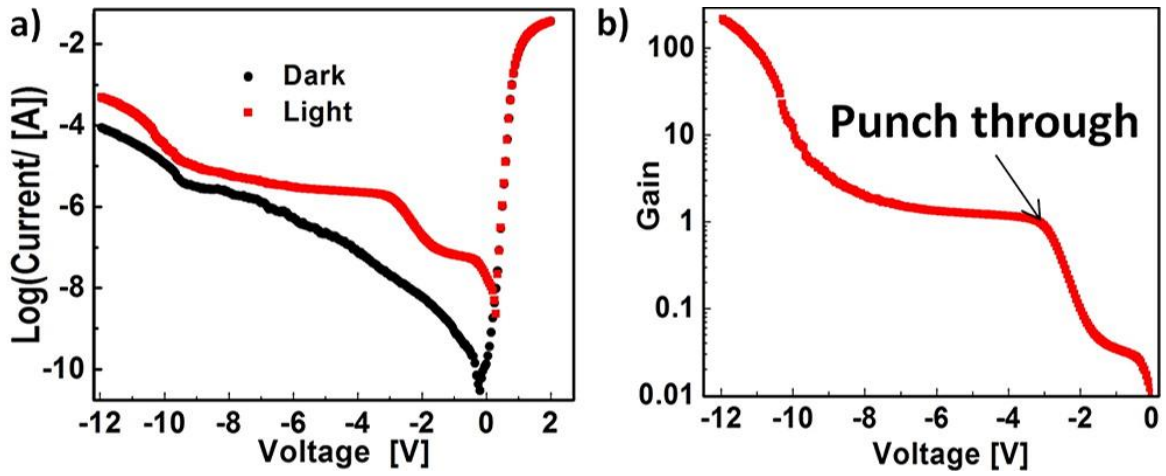

Figure 18: a) Light and dark I-V characteristic and b) the multiplication of GaAs core-shell diode

Figure 18(b) shows the gain characteristic calculated by subtracting the dark current from the light current and normalizing with respect to the primary photocurrent at the onset of the plateau region. The unity gain primary photocurrent is measured at −3.2 V. Increased reverse bias results in a monotonic increase in avalanche gain until gains as high as ~216 can be achieved at −12 V due to avalanche multiplication in Fig. 18(b).

A deeper understanding of the measured gain characteristics and a correlation with the volume of the avalanche region can be obtained from modeling the capacitance–voltage (*C*–*V*) measurements using the doping and the geometry of the nanopillar. The best fit for the *C*–*V* characteristic can be used to estimate the high electric field volume responsible for the avalanche gain. Figure 19 shows capacitance (*C*–*V*) characteristics as a function of area at a high frequency

of 1 MHz to sample purely the junction capacitance. The capacitance scales with area indicating that the junction capacitance of each nanopillar is acting in parallel and a very high uniformity in the formation of the core–shell PN junction in the nanopillar array. At zero bias the capacitance due to the core–shell junction is ~0.347 fF/μm^2. A small reverse bias of −1 V results in a ~50% drop in the capacitance, until higher reverse biases results in the saturation of the capacitance to ~0.05 fF/μm$^{2.}$ We roughly estimate that this ultrasmall saturation capacitance would allow nanopillar diode arrays, with as few as 3000 NPs to have a RC limited bandwidth exceeding 40 GHz.

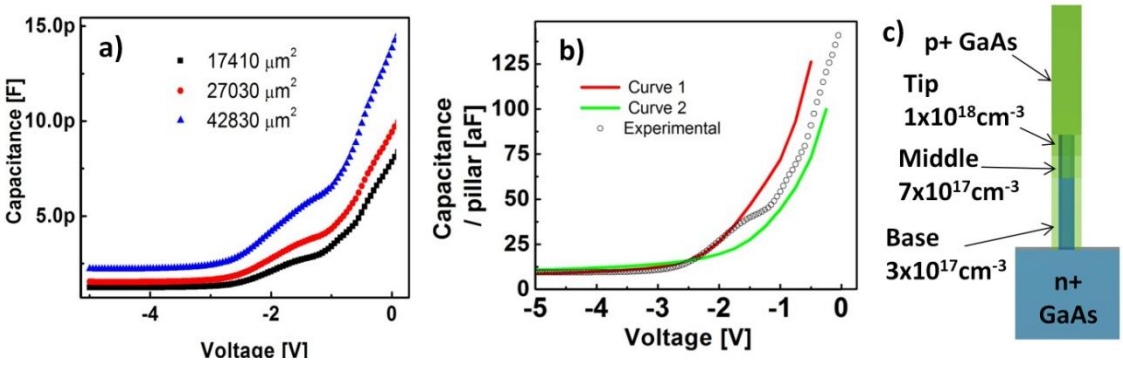

Figure 19: a) Capacitance-Voltage (CV) characteristics of nanopillar arrays with different number of nanopillars b) Extracted average capacitance per nanopillar compared with a modelled capacitance c) Schematic of the structure used for 3D modeling of capacitance

Figure 19(b) shows the average capacitance per nanopillar overlaid with C-V modeling (Curves 1 and 2) of the NP core-shell junction. The average junction capacitance per nanopillar can be estimated by subtracting the contribution to the capacitance due to BCB and dividing by the number of NPs in the array. The modeled C-V curves are generated by solving the 3D Poisson equations [65] taking into account the core-shell geometry and doping of the hexagonal nanopillar. In both Curves 1 and 2 the modeled core is 80 nm in diameter and 800 nm in height and uniformly doped n-type at a doping concentration of 3x10^{18} cm^{-3}. The doping of the p-type

doped shell is coarsely graded, i.e. divided into three sections including base, middle and tip accounting for expected growth rate changes during nanopillar epitaxy (Fig. 19(c)).[52, 66] The doping concentration within the base, middle and tip sections are constant at $3x10^{17}$ cm^{-3}, $7x10^{17}$ cm^{-3} and $1x10^{18}$ cm^{-3}, respectively. However, the CV characteristics are very sensitive to the thickness of the middle section surrounding the tip of the core. Thus, Curve 1 (2) represent a base section spanning 500 nm (600 nm), the middle section of 150 nm (100 nm), and the tip at

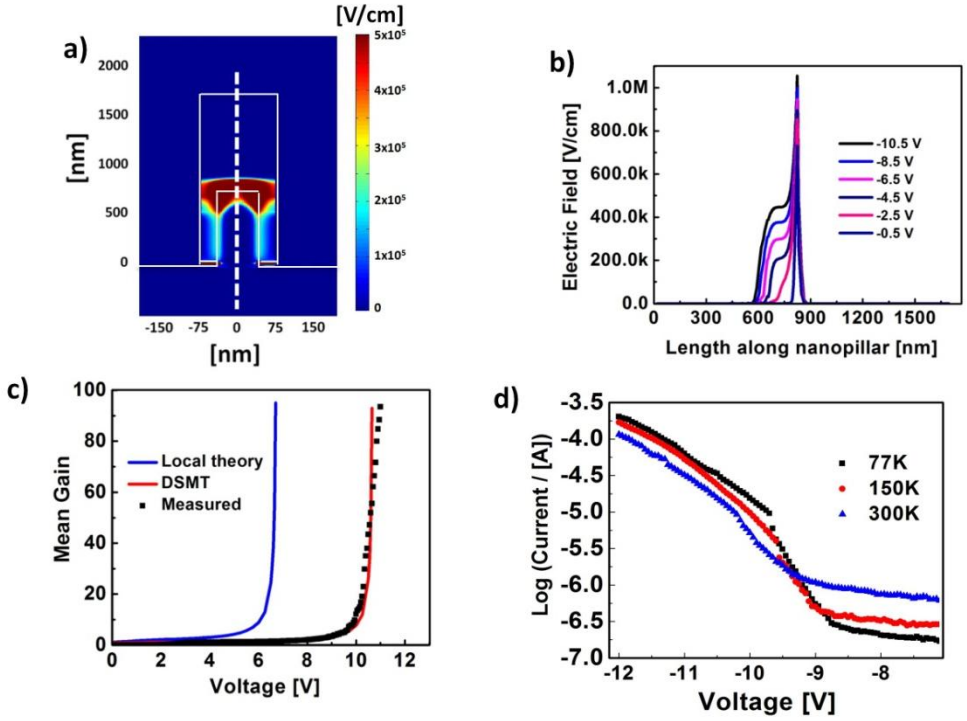

Figure 20: a) Contour plot of the electric field in the nanopillar at -10 V b) Axial electric field profile along the pillar as a function of reverse bias. c) Calculated gain using local and DSMT compared with experimental gain d) Shows the characteristic temperature dependence of avalanche breakdown

150 nm (100 nm).

A clear trend can be seen in that the peak capacitance at low bias voltages drops as the size of the high doped region encapsulating the tip of the core is reduced, while the saturation capacitance also increases. Curve 1 is chosen to most accurately represent the characteristics of the device in terms of accurately predicting the punch through voltage, the shape of the CV characteristic and the saturation capacitance C_{sat} ~ 9 aF. The CV characteristic of Curve 1 can be understood as the radial expansion of the 3D depletion region by initially depleting the core-shell junction and then extending axially to the pillar edge. At the bias voltage of -5 V the depletion region has expanded axially resulting in the saturation of the capacitance at ~ 9 aF for a single nanopillar.

Figure 20(a) shows a contour plot of the electric field through the center of the nanopillar (in the x-plane) at the breakdown voltage of -10V. The graded doping of the p-shell results in the high field ($E > 5x10^5$ V/cm) region being confined to within 310 nm of the tip of the core. Since very high electric fields are confined to within a very small region of the core-shell junction the resulting impact ionization is also being confined to a very small volume. The thin avalanche volume results in the measured gain characteristics to be dominated by dead space effects.

Figure 20(b) shows the axial electric-field profiles as a function of reverse bias through the center of the nanopillar (at the location of the dotted white line in Figure 20(a)) for the structure described by Curve 1. The avalanche region at the breakdown voltage is confined to an axial region ~310 nm in width with highly localized fields as high as 1 MV/cm at the tip of the nanopillar core. The bias dependent electric field profiles can be used to model the expected gain

using both local theory for carrier multiplication[67] and dead space multiplication theory[9]. It is expected that modeling the gain in terms of dead space multiplication theory (DSMT) would lower the mean gain at a given bias and shift the breakdown voltage to higher biases. In both cases, it is assumed that a majority of carriers contributing to avalanche multiplication traverse a path through the center of the nanopillar as shown by the white dotted line in Figure 20(a). In terms of the local theory the mean multiplication (M) is given using Eq. 5 below, where α is the electron ionization coefficient, β is the hole ionization coefficient, and is evaluated at $x = W$ where W is the position of the depletion edge.

$$M(x_0) = \frac{\exp\left[-\int_0^{x_0}\left(\alpha(x)-\beta(x)\right)dx\right]}{1-\int_0^{W}\alpha(x)\exp\left[-\int_0^{x}\left(\alpha(x')-\beta(x')\right)dx'\right]dx} \qquad (5)$$

For the case of DSMT the electric-field profiles in Fig. 20(b) were also used to calculate the dead-space profiles across the nanopillar and the non-local ionization coefficients for electrons and holes in GaAs as described by Saleh *et al.*[14] With this information we calculate the probability density functions of the random distance of ionization for electrons and holes. A hard-threshold dead space is assumed, for which the ionization coefficient is zero for carriers that have traveled a distance shorter than the dead space and is a function of the electric field for carriers that have traveled a longer distance.

Figure 20(c) shows the calculated gain using local theory and DSMT using the electric fields of Curve 1 overlaid with the experimental gain. Local theory is shown to produce an over estimation to the measured gain resulting in an under estimation of the breakdown voltage. However, the mean gain estimated by DSMT is able to predict the experimental gain and

breakdown voltage more accurately than the local theory, since the effect of the dead space are significant.

Figure 20(d) shows the temperature dependent I-V characteristics of the core-shell NP diodes at high reverse biases from 77K to 300K. All curves show similar behavior: a clear transition from a generation-recombination dominated current to an avalanche current close to the breakdown voltage at ~ 9.5 V. The breakdown voltage is consistent with the predictions of the DSMT. This dramatic change in the I-V characteristic suggests that dark carriers injected into the high-field core-shell region are multiplied. The breakdown voltage can be calculated by extracting the voltage at which multiplication (M) goes to infinity. The unmultiplied dark current is taken to be -7 V from which the multiplication factor M is calculated. The intersection of 1/M vs. bias is used to estimate the breakdown voltage at each temperature (See Supporting Information). The breakdown voltage shifts to larger biases with increasing temperature with a shift of +3.3 mV/K, such a small shift in the breakdown voltage suggests that the avalanche gain is produced by a high field region on the order of the ionization path length of electrons as higher temperatures result in greater energy scattering of carriers. The clear shift in the breakdown voltage is in stark contrast to previous reports of GaAs nanowire APDs where a positive shift in the breakdown voltage is not clearly observed.[68]

Excess noise characterization of GaAs 3D-NOAADs

GaAs 3D NOAADs were characterized for gain and excess noise factors in collaboration with Prof. Siddhartha Ghosh at University of Illinois Chicago. Devices were probed using a Janis 500 T cryogenic probe station at 300 K such that DC bias was applied using a bias-tee and AC noise was measured using a Agilent 8973b noise meter. Optical illumination was provided using

a He-Ne laser calibrated to output ~ 200 μW. Unity gain was calculated from Fig. 18(b) after punch through of the depletion region into the absorption region.

Figure 21 shows the measured excess noise factor a function of multiplication gain in the GaAs nanopillar avalanche detectors. At low gains the extracted excess noise factor is dominated by

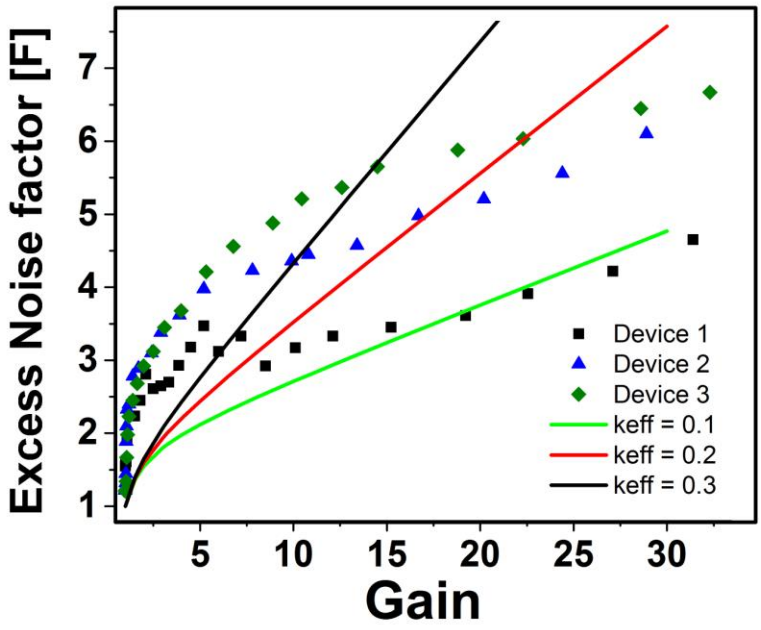

Figure 21: Excess noise factor vs. Gain for GaAs NOAAD fitted with Mcyntyre fitting of keff

the output noise of the preamplifier. However, at higher gains the excess noise factor approaches fits to the McIntyre equation. Several devices from the same nanopillar growth run have been measured and similar low excess noise has been observed. The measured excess noise factors are well below the ratio of the ionization coefficients reported for GaAs bulk avalanche detectors. The effective ratio of ionization coefficients for electrons to holes is measured to be less than 0.1. For bulk GaAs, the ratio is close to 1[3]. Low excess noise factors (keff ~ 0.3) have been measured in bulk GaAs diodes

where the multiplication region ~ 100 nm. The physical origin of such a low excess noise factor is still being investigated using dead space multiplication theory (DSMT).

4.0 InGaAs-GaAs heterojunction NOAADs

Incorporating indium (In) within the nanopillar during the GaAs nanopillar allows the extension of the cut-off wavelength to the 1 - 1.3 µm range[41]. Lattice mismatched InGaAs nanopillar arrays were grown by selective area epitaxy metal organic vapor phase epitaxy on GaAs substrates as shown in Fig. 22(a). The nanopillars were passivated by wide bandgap InGaP shells to reduce surface related dark current densities resulting in uniform arrays as shown in Fig. 22(b) and (c). The nanopillar arrays were fabricated into high speed APDs with GSG contact pads utilizing self aligned metal hole array antenna for the signal contact as shown in Fig. 22(d) and (e).

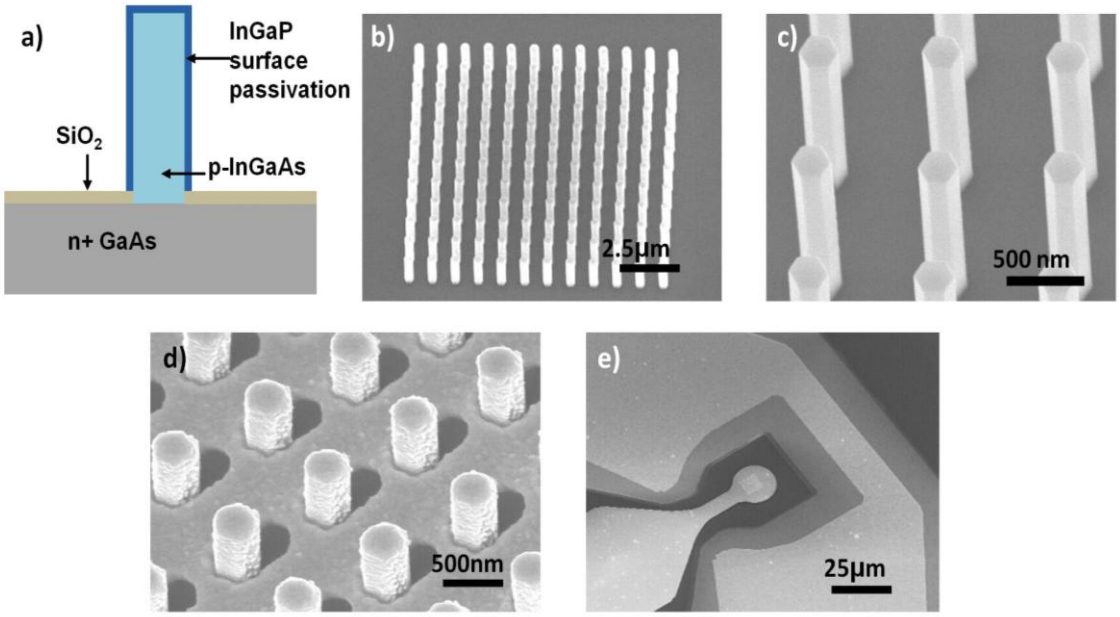

Figure 22: a) Schematic of nanopillar structure investigated for 1 micron nanopillar APD b) SEM of 10 µm x 10 µm array c) Close up view of InGaAs nanopillar passivated with InGaP d) Close up SEM of final device showing plasmonic metal hole array antenna e) Nanopillar array integrated with GSG contact pads

properties of the APDs were investigated by current voltage (IV) measurements under dark and under light as shown in Figure 23. Sample AF024 was grown such that the Indium composition

36%, p-type Zinc doping of ~ $10^{17}cm^{-3}$. Sample AF025 has an Indium composition 36%, p-type Zinc doping of ~ $10^{18}cm^{-3}$. Sample AF026 has a Indium composition 27%, p-type Zinc doping of ~ $10^{17}cm^{-3}$

All photocurrent measurements performed with a fiber coupled 1060nm laser calibrated to 21 μW of incident optical power. The device characteristics of three growths are reported

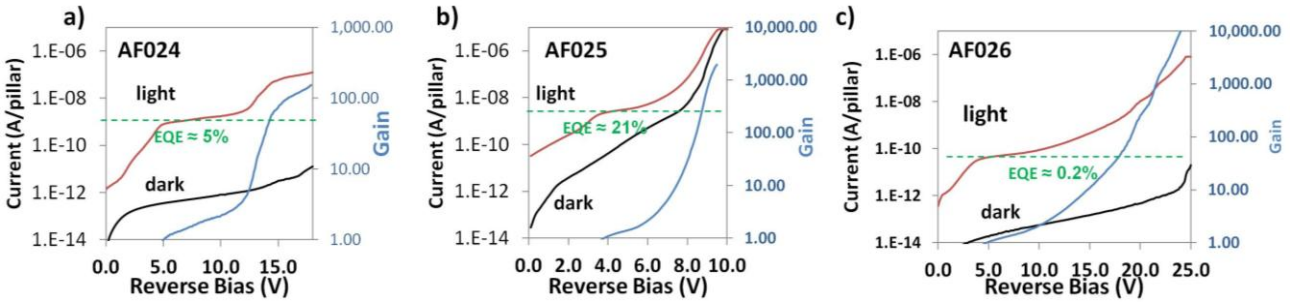

Figure 23: Light dark current voltage and gain characteristics of InGaAs nanopillar APDs a) sample AF024 b) sample AF025 c) sample AF026

here. The dark IV characteristics show that increasing the doping of the nanopillar lowers the breakdown voltage (~ 9 V) with increased dark current (2.38 nA/pillar @ M = 10), while lower doping concentrations produces higher breakdown voltages (~ 20 V) with lower dark currents (1.37 pA/pillar @ M = 10). Reducing the indium composition of the nanopillar is also shown to reduce dark current (143 fA/pillar @ M = 10) and increase the breakdown voltage. In terms of the performance of the devices under light, the best combination of gain and quantum efficiency was observed for device in Fig. 23b) with a ***unity gain quantum efficiency of 21% and a maximum gain of 1430.***

4.1 Electric field of InGaAs-NOAADs

As shown earlier the avalanche breakdown characteristics of InGaAs NOAADs are heavily dependent of the doping profile of the nanopillar. A detailed analysis of the capacitance

voltage characteristics are performed to extract doping concentrations within the nanopillar. The InGaAs nanopillar, GaAs substrate, the geometry of the top contact and the in-filling BCB layer is modeled in Sentaurus. The doping concentration of the InGaAs nanopillar is varied from 1 x 10^{18} cm^{-3} at the base to 5 x 10^{18} cm^{-3} at the tip. The extracted fit to the experimental capacitance is shown in Fig. 24(a). Fig. 24(b) shows the 3D electric field distribution of the InGaAs nanopillar GaAs substrate heterojunction. It should be noted that the BCB planarization layer smears out the field at the substrate nanopillar junction, similar to the breakdown characteristics observed by in silicon nanowire pn junctions[1]. Since the p-doped InGaAs region has a doping gradient a quasi electric field is created which aids in extraction of photogenerated electrons into

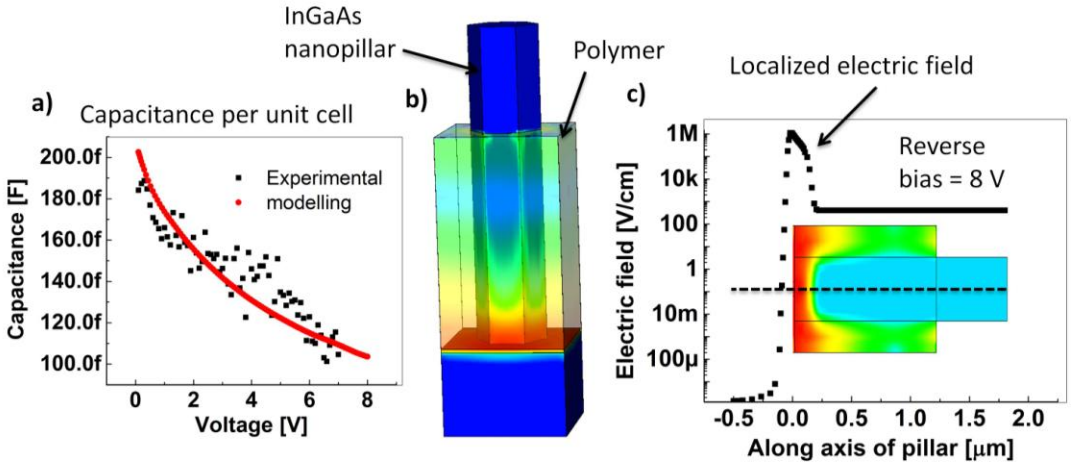

Figure 24: a) Fitting of the experimental CV characteristics b) 3D electric field profile including dielectric polymer layer c) 1-D electric through the center of the nanopillar. Inset shows a electric field in the x-z plane

the multiplication region. At 8 V reverse bias the high field region is confined to within a ~ 200 nm from the base of the pillar as shown in Fig. 24(c). The drift electric field in the absorption region reaches ~ 400 V/cm, which is sufficiently high to cause carriers to drift[64] into the multiplication region, instead of recombining.

4. 1 Excess noise characterization of InGaAs NOAADs

InGaAs NOAADs are characterized for excess noise gain characteristics using custom setup built at UCLA. The main technical challenge to be overcome in making noise measurements is to accurately attribute the measured noise to the device under test as opposed to external noise sources such as DC power supplies, preamplifier noise, unshielded cables and laser induce Relative Intensity Noise. High speed GSG contact pads reduces the contribution to the noise signal from external sources. Low noise DC bias is provided by the Agilent B2962A through the picosecond pulse labs model 5543 bias T. The AC current noise is amplified by the low noise current preamplifier Stanford Research model SR570 and spectral noise density is displayed using the Stanford Research FFT signal analyzer model SR780. The noise current density is

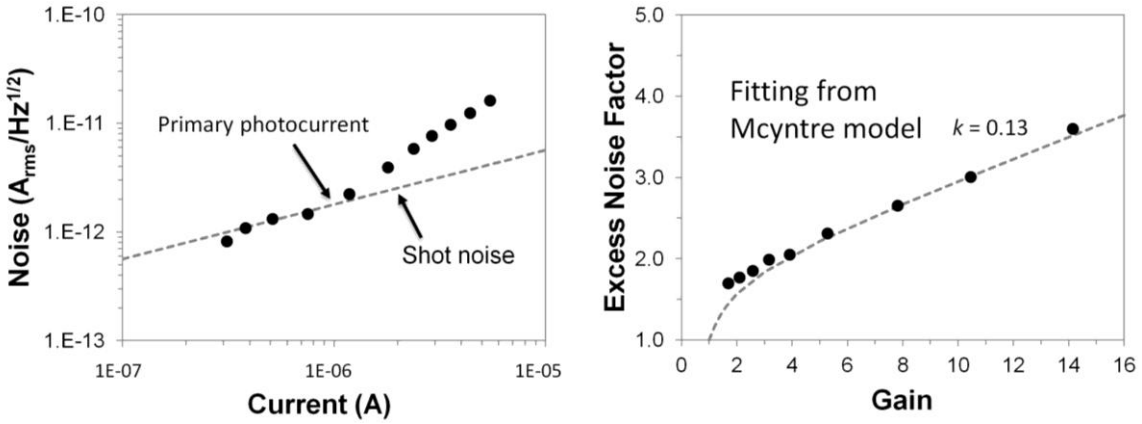

Figure 25: Noise Spectral Density (NSD) vs. photocurrent b) Excess noise factor vs. Gain (M)

extracted from the "flat region" of the noise spectrum beyond the 1/f noise knee. Light is coupled into the APD using a multimode lensed fiber with a spot size ~ 50 μm coupled to a pigtailed fiber laser with a FC termination. Shot noise of the DC photocurrent is confirmed below unity gain as shown in Fig. 26a) fitting the relationship $i_{ns} = \sqrt{2qI_{ph}}$. With increasing photocurrent the

current noise spectral density increases beyond the shot noise floor. The increased noised can be quantified in terms of an excess noise factor (F), such that $F = \frac{S_{ph}}{2qI_{ph}M^2}$ [69]. The onset of avalanche gain at low electric fields can be hidden by the movement of the depletion edge with increased bias improving carrier collection. The bias voltage for the additional noise beyond the shot noise floor was used to identify unity gain as shown in Fig. 25(a)[70]. Fig. 25(b) shows the excess noise vs. Gain and the fitting to Mcyntre's k_{eff} described in Section 1. Excess noise factors for the InGaAs 3D NOAADs are significantly less that bulk InGaAs APDs[70] where k_{eff} approached unity as the multiplication region width is less that 1 micron.

4. 2 Gain-bandwidth characterization of InGaAs NOAADs

The bandwidth of APDs can either be transit-time limited or RC-limited depending on the fabrication scheme of the device. Emmons[71] showed for transit time limited APDs the bandwidth would reduce as soon as the gain (M) > 1 / k_{eff}. However, in the case of the InGaAs NOAADs the devices were not fabricated on semi-insulating substrates to reduce parasitic capacitances, and therefore RC-limited. The signal contact being deposited on top of the BCB creates a parasitic capacitance of ~ 280 fF, together with a series resistance of ~ 220 Ω produces a RC limited bandwith of 2.6 GHz. Impulse response and associated DC gain of typical InGaAs NOAAD devices are shown in Fig. 26 below. DC gains as high as 982 are achieved at a reverse bias of 7.6 V as shown in Fig. 26(a). From the impulse response measurements shown in Fig. 26(b) the response of the InGaAs NOAADs are non-gaussian with a fast rise time (~17 ps) and a significantly slower fall time (~ 90 ps). The bandwidth of the InGaAs NOAAD is essentially limited by the fall time, which is attributed to the RC time constant of parasitic BCB capacitance.

A maximum gain bandwidth product of 2.8 GHz x 711 = 2 THz. Such high gain-bandwidth products is exceptionally high compared to APDs fabricated from bulk InGaAs[70].

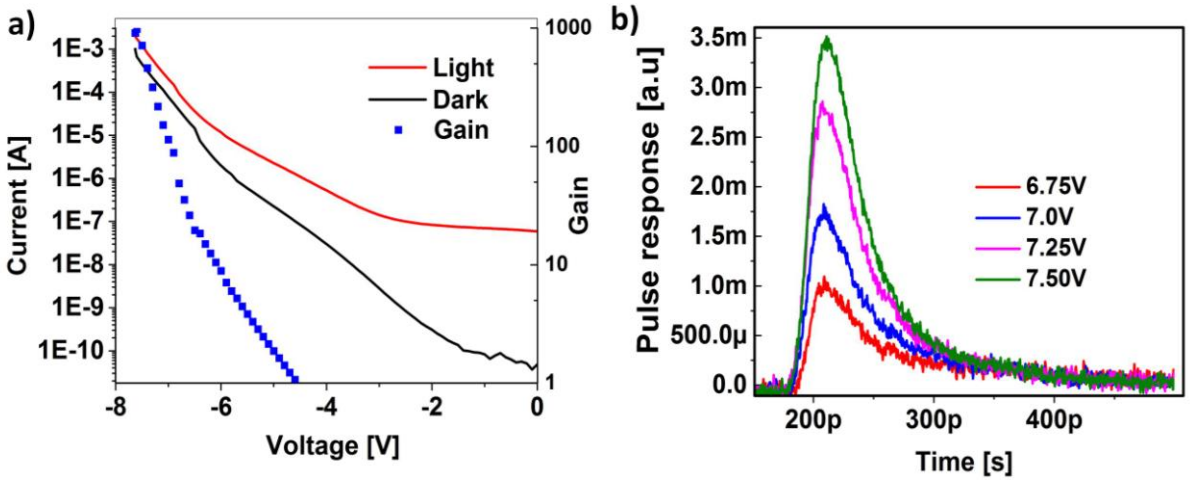

Figure 26: Dark/light IV characteristics of InGaAs NOAAD b) Impulse response of InGaAs NOAAD to 80 fs Ti-sapphire laser

5.0 Future outlook

The devices realized in this thesis demonstrate the proof of concept of NOAADs in accomplishing wavelength tunable, low operating bias, high gain, low excess noise and high speed avalanche photodetectors. Further improvements can be made to engineer the electric field of the NOAAD, such that high gains can be achieved with lower dark currents (< 1 nA at M > 10). The mechanisms for dark current generation needs to be studied by varying the nanohole diameter to isolate bulk and surface induced dark current. This is particularly challenging in nanopillars grown by selective area epitaxy since the growth conditions of the nanopillar changes with the size of the electron beam defined nanohole. InP, InAs and InAlAs nanopillars / core-shell structures can also be explored as candidate materials for multiplication regions, which would potentially reduce dark currents. In terms of commercial application to LADAR focal plane arrays, NOAADs need to be integrated with planar epitaxy on (111) substrates to achieve hybridization with silicon Read out Integrated Circuits. The physical origin for the exceptionally high gain-bandwidth product reported in this work can be further explored in terms of impact ionization modeling of the 3D photogeneration rates and electric fields.

References

1. Agarwal, P.; Vijayaraghavan, M. N.; Neuilly, F.; Hijzen, E.; Hurkx, G. A. M. *Nano Lett.* **2007,** 7, (4), 896-899.
2. Assefa, S.; Xia, F.; Vlasov, Y. A. *Nature* **2010,** 464, (7285), 80-84.
3. Bulman, G. E.; Robbins, V. M.; Stillman, G. E.; Stillman, G. E. *Electron Devices, IEEE Transactions on* **1985,** 32, (11), 2454-2466.
4. Okamoto, D.; Fujikata, J.; Ohashi, K. *Jpn J Appl Phys* **2011,** 50, (12), 120201-120201-3.
5. Asbrock, J.; Bailey, S.; Baley, D.; Boisvert, J.; Chapman, G.; Crawford, G.; de Lyon, T.; Drafahl, B.; Edwards, J.; Herrin, E.; Hoyt, C.; Jack, M.; Kvaas, R.; Liu, K.; McKeag, W.; Rajavel, R.; Randall, V.; Rengarajan, S.; Riker, J. In *Ultra-High sensitivity APD based 3D LADAR sensors: linear mode photon counting LADAR camera for the Ultra-Sensitive Detector program*, 2008; 2008; pp 69402O-69402O-16.
6. McIntyre, R. J. *Electron Devices, IEEE Transactions on* **1966,** 13, (1), 164-168.
7. Hu, C.; Anselm, K. A.; Streetman, B. G.; Campbell, J. C. *Appl. Phys. Lett.* **1996,** 69, (24), 3734-3736.
8. Saleh, M. A.; Hayat, M. M.; Sotirelis, P. P.; Holmes, A. L.; Campbell, J. C.; Saleh, B. E. A.; Teich, M. C. *Electron Devices, IEEE Transactions on* **2001,** 48, (12), 2722-2731.
9. Hayat, M. M.; Saleh, B. E. A.; Teich, M. C. *Electron Devices, IEEE Transactions on* **1992,** 39, (3), 546-552.
10. Li, K. F.; Ong, D. S.; David, J. P. R.; Rees, G. J.; Tozer, R. C.; Robson, P. N.; Grey, R. *Electron Devices, IEEE Transactions on* **1998,** 45, (10), 2102-2107.
11. Plimmer, S. A.; Tan, C. H.; David, J. P. R.; Grey, R.; Li, K. F.; Rees, G. J. *Appl. Phys. Lett.* **1999,** 75, (19), 2963-2965.
12. Williams, G. M.; Huntington, A. S. In *Probabilistic analysis of linear mode vs. geiger mode APD FPAs for advanced LADAR enabled interceptors*, 2006; 2006; pp 622008-622008-14.
13. Zheng, X. G.; Hsu, J. S.; Hurst, J. B.; Li, X.; Wang, S.; Sun, X.; Holmes, A. L.; Campbell, J. C.; Huntington, A. S.; Coldren, L. A. *IEEE J. Quantum Electron.* **2004,** 40, (8), 1068-1073.
14. Williams, G. M.; Huntington, A. S. *Proc. SPIE - Int. Soc. Opt. Eng.* **2006,** 6220, (1), 622008-1-14.
15. Lenox, C.; Nie, H.; Yuan, P.; Kinsey, G.; Homles, A. L., Jr.; Streetman, B. G.; Campbell, J. C. *Photonics Technology Letters, IEEE* **1999,** 11, (9), 1162-1164.
16. Albota, M. A.; Aull, B. F.; Fouche, D. G.; Heinrichs, R. M.; Kocher, D. G.; Marino, R. M.; Mooney, J. G.; Newbury, N. R.; O'Brien, M. E.; Player, B. E.; Willard, B. C.; Zayhowski, J. J. *Linc. Lab. J.* **2002,** 13, (2), 351-370.
17. Heinrichs, R. M.; Aull, B. F.; Marino, R. M.; Fouche, D. G.; McIntosh, A. K.; Zayhowski, J. J.; Stephens, T.; O'Brien, M. E.; Albota, M. A. *Proc. SPIE - Int. Soc. Opt. Eng.* **2001,** 4377, 106-17.
18. Knight, M. W.; Sobhani, H.; Nordlander, P.; Halas, N. J. *Science* **2011,** 332, (6030), 702-704.
19. Chang, C.-C.; Sharma, Y. D.; Kim, Y.-S.; Bur, J. A.; Shenoi, R. V.; Krishna, S.; Huang, D.; Lin, S.-Y. *Nano Lett.* **2010,** 10, (5), 1704-1709.

20. Collin, S.; Vincent, G.; Haïdar, R.; Bardou, N.; Rommeluère, S.; Pelouard, J.-L. *Physical Review Letters* **2010,** 104, (2), 027401.
21. Ghaemi, H. F.; Thio, T.; Grupp, D. E.; Ebbesen, T. W.; Lezec, H. J. *Physical Review B* **1998,** 58, (11), 6779-6782.
22. Degiron, A.; Ebbesen, T. W. *Journal of Optics a-Pure and Applied Optics* **2005,** 7, (2), S90-S96.
23. Williams, S. M.; Stafford, A. D.; Rogers, T. M.; Bishop, S. R.; Coe, J. V. *Appl. Phys. Lett.* **2004,** 85, (1472-1474).
24. Martin-Moreno, L.; Garcia-Vidal, F. J.; Lezec, H. J.; Pellerin, K. M.; Thio, T.; Pendry, J. B.; Ebbesen, T. W. *Physical Review Letters* **2001,** 86, (6), 1114-1117.
25. Dintinger, J.; Klein, S.; Bustos, F.; Barnes, W. L.; Ebbesen, T. W. *Physical Review B* **2005,** 71, (3).
26. Barnes, W. L.; Murray, W. A.; Dintinger, J.; Devaux, E.; Ebbesen, T. W. *Physical Review Letters* **2004,** 92, (10).
27. Genet, C.; Ebbesen, T. W. *Nature Photonics* **2007,** 445, 39-46.
28. Garcia-Vidal, F. J.; Lezec, H. J.; Ebbesen, T. W.; Martin-Moreno, L. *Physical Review Letters* **2003,** 90, (21).
29. Garcia-Vidal, F. J.; Martin-Moreno, L.; Lezec, H. J.; Ebbesen, T. W. *Applied Physics Letters* **2003,** 83, (22), 4500-4502.
30. Lezec, H. J.; Degiron, A.; Devaux, E.; Linke, R. A.; Martin-Moreno, L.; Garcia-Vidal, F. J.; Ebbesen, T. W. *Science* **2002,** 297, (5582), 820-822.
31. Martin-Moreno, L.; Garcia-Vidal, F. J.; Lezec, H. J.; Degiron, A.; Ebbesen, T. W. *Physical Review Letters* **2003,** 90, (16).
32. Brolo, A. G.; Gordon, R.; Leathem, B.; Kavanagh, K. L. *Langmuir* **2004,** 20, 4813-4815.
33. Liu, Y.; Blair, S. *Opt. Lett.* **2003,** 28, 507-509.
34. Tang, L.; Latif, S.; Miller, D. A. B. *Elec. Lett.* **2009,** 45.
35. Tang, L.; Miller, D. A. B.; Okyay, A. K.; Matteo, J. A.; Yuen, Y.; Saraswat, K. C.; Hesselink, L. *Opt. Lett.* **2006,** 31, 1519-1521.
36. Ishi, T.; Fujikata, J.; Makita, K.; Baba, T.; Ohashi, K. *Jpn. J. Appl. Phys.* **2005,** 44, L364-L366
37. Lee, S. C.; Krishna, S.; Brueck, S. R. J. *IEEE Photon. Tech. Lett.* **2011,** 23, 935-937.
38. Rosenberg, J.; Shenoi, R. V.; Krishna, S.; Painter, O. *Opt. Express* **2010,** 18, 3672-3686.
39. Shackleford, J. A.; Grote, R.; Currie, M.; Spanier, J. E.; Nabet, B. *Appl. Phys. Lett.* **2009,** 94, 083501.
40. OKAMOTO, D.; FUJIKATA, J.; NISHI, K.; OHASHI, K. *Jpn. J. Appl. Phys.* **2008,** 47, 2921-2923.
41. Senanayake, P.; Hung, C. H.; Shapiro, J.; Lin, A.; Liang, B. L.; Williams, B. S.; Huffaker, D. L. *Nano Letters* **2011,** 11, (12), 5279-5283.
42. Martyniuk, P.; Rogalski, A. *Opto-Electron. Rev.* **2013,** 21, (2), 239-257.
43. Barnes, W. L.; Dereux, A.; Ebbesen, T. W. *Nature* **2003,** 424, (6950), 824-830.
44. Koerkamp, K. J. K.; Enoch, S.; Segerink, F. B.; van Hulst, N. F.; Kuipers, L. *Physical Review Letters* **2004,** 92, (18), 4.
45. Bouchon, P.; Pardo, F.; Portier, B.; Ferlazzo, L.; Ghenuche, P.; Dagher, G.; Dupuis, C.; Bardou, N.; Haidar, R.; Pelouard, J.-L. *Appl. Phys. Lett.* **2011,** 98, (19), 191109-3.

46. Senanayake, P.; Hung, C.-H.; Shapiro, J.; Scofield, A.; Lin, A.; Williams, B. S.; Huffaker, D. L. *Opt. Express* **2012,** 20, (23), 25489-25496.
47. Takei, K.; Fang, H.; Kumar, S. B.; Kapadia, R.; Gao, Q.; Madsen, M.; Kim, H. S.; Liu, C.-H.; Chueh, Y.-L.; Plis, E.; Krishna, S.; Bechtel, H. A.; Guo, J.; Javey, A. *Nano Lett.* **2011,** 11, (11), 5008-5012.
48. Miller, L. M.; Smith, R. J. *Vibrational Spectroscopy* **2005,** 38, (1–2), 237-240.
49. Nicolet Continuμm Infrared Microscope. In Thermo Scientific: p 12.
50. Kim, T. J.; Ghong, T. H.; Kim, Y. D.; Kim, S. J.; Aspnes, D. E.; Mori, T.; Yao, T.; Koo, B. H. *Physical Review B* **2003,** 68, (11), 10.
51. Adachi, S., *Properties of aluminium gallium arsenide*. INSPEC: 1993
52. Shapiro, J. N.; Lin, A.; Wong, P. S.; Scofield, A. C.; Tu, C.; Senanayake, P. N.; Mariani, G.; Liang, B. L.; Huffaker, D. L. *Appl. Phys. Lett.* **2010,** 97, (24), 243102-243102-3.
53. Knight, M. W.; Sobhani, H.; Nordlander, P.; Halas, N. J. *Science* 332, (6030), 702-704.
54. Catchpole, K. R.; Polman, A. *Appl. Phys. Lett.* **2008,** 93, (19), 191113-3.
55. Mokkapati, S.; Beck, F. J.; Waele, R. d.; Polman, A.; Catchpole, K. R. *Journal of Physics D: Applied Physics* **2011,** 44, (18), 185101.
56. Senanayake, P.; Hung, C.-H.; Shapiro, J.; Lin, A.; Liang, B.; Williams, B. S.; Huffaker, D. L. *Nano Lett.* **2011,** 11, (12), 5279-5283.
57. Yu, K.; Lakhani, A.; Wu, M. C. *Opt. Express* **2010,** 18, (9), 8790-8799.
58. Gao, H.; Zhou, W.; Odom, T. W. *Advanced Functional Materials* 20, (4), 529-539.
59. Williams, S.; Coe, J. *Plasmonics* **2006,** 1, (1), 87-93.
60. Rosenberg, J.; Shenoi, R. V.; Krishna, S.; Painter, O. *Opt. Express* **2010,** 18, (4), 3672-3686.
61. Gao, H.; Zhou, W.; Odom, T. W. *Advanced Functional Materials* **2009,** 20, (4), 529-539.
62. Hiskett, P. A.; Buller, G. S.; Loudon, A. Y.; Smith, J. M.; Gontijo, I.; Walker, A. C.; Townsend, P. D.; Robertson, M. J. *Appl. Opt.* **2000,** 39, (36), 6818-6829.
63. Scofield, A. C.; Shapiro, J. N.; Lin, A.; Williams, A. D.; Wong, P.-S.; Liang, B. L.; Huffaker, D. L. *Nano Lett.* **2011,** 11, (6), 2242-2246.
64. Graham, R.; Miller, C.; Oh, E.; Yu, D. *Nano Lett.* **2010,** 11, (2), 717-722.
65. Chi-Kang, L.; Yuh-Renn, W. *Electron Devices, IEEE Transactions on* **2012,** 59, (2), 400-407.
66. Allen, J. E.; Perea, D. E.; Hemesath, E. R.; Lauhon, L. J. *Advanced Materials* **2009,** 21, (30), 3067-3072.
67. Stillman, G. E.; Wolfe, C. M., *Semiconductors and Semimetals*. 1977; Vol. 12.
68. Chuang, L. C.; Sedgwick, F. G.; Chen, R.; Ko, W. S.; Moewe, M.; Ng, K. W.; Tran, T.-T. D.; Chang-Hasnain, C. *Nano Lett.* **2010,** 11, (2), 385-390.
69. Xie, F. Z.; Kuhl, D.; Bottcher, E. H.; Ren, S. Y.; Bimberg, D. *Journal of Applied Physics* **1993,** 73, (12), 8641-8646.
70. Yu Ling, G.; Jo Shien, N.; Chee Hing, T.; Ng, W. K.; David, J. P. R. *Photonics Technology Letters, IEEE* **2005,** 17, (11), 2412-2414.
71. Emmons, R. B. *Journal of Applied Physics* **1967,** 38, (9), 3705-3714.